Probabilistic assessment of tropical cyclone recovery burden across US Atlantic and Gulf Coast counties

Simona Meiler[1], Nikola Blagojević[1], Meredith Lochhead[1], Avantika Gori[2], and Jack W. Baker[1]

[1]Department of Civil and Environmental Engineering, Stanford University, Stanford, CA, USA
[2]Department of Civil and Environmental Engineering, Rice University, Houston, TX, USA

Correspondence: Simona Meiler (simona@simonameiler.ch)

This manuscript is a non-peer-reviewed preprint submitted to EarthArXiv. It is intended for submission to Natural Hazards and Earth System Sciences for peer review. The content has not yet undergone peer review and may be subject to revision.

Abstract. Tropical cyclones cause widespread damage to housing and infrastructure, and recovery is often slow and uneven. Climate risk assessments quantify the likelihood and direct impacts of extreme events, but post-disaster recovery remains largely absent from these models, limiting our ability to assess long-term resilience. We therefore integrate simplified recovery modeling into probabilistic tropical cyclone risk assessment for all counties along the US Atlantic and Gulf coasts. We quantify county-level repair demand for residential buildings using a large synthetic set of tropical cyclone events and compare it with baseline local construction capacity, proxied by residential building permits. The resulting recovery burden expresses the modeled repair workload in months of baseline construction activity. The relative importance of repair demand and construction capacity depends on how recovery burden is summarized. Expected annual recovery burden is dominated by rare, high-impact events and closely tracks the expected annual repair demand. For the median damaging event in each county, construction capacity becomes more important, and counties with comparable repair demands can face substantially different recovery burdens. A joint screening identifies 60 high-risk, low-capacity counties that are particularly susceptible to post-disaster construction bottlenecks. Incorporating baseline construction capacity into risk assessment can therefore inform where reconstruction support would complement efforts to reduce tropical cyclone risk.

1 Introduction

Restoring housing and infrastructure after a disaster can extend over years and differ substantially across affected communities. After Hurricane Maria (2017), Puerto Rico experienced the longest blackout in US history, with more than 4 billion customer hours of interruption and large disparities in electricity restoration across municipalities and neighborhoods (Román et al., 2019). The 2018 Camp Fire destroyed 18,804 structures in Paradise, California, and displaced most residents; by 2021, active residential addresses had recovered to only about one quarter of their pre-fire level (Knapp et al., 2021; Din, 2022). Recovery speed after such events varies widely across communities that suffer comparable damage, because rebuilding depends not only on the physical extent of damage but also on the capacity to organize, finance, and complete reconstruction (Johnson and Olshansky, 2017; Markhvida et al., 2020). A more complete picture of climate risk and resilience therefore requires considering recovery alongside the direct impacts of extreme events (Bruneau et al., 2003; Cutter et al., 2008).

Climate risk assessments, however, typically quantify the immediate loss of functionality caused by an event. Depending on the system of interest, this loss can be represented as damaged buildings and infrastructure (Ward et al., 2020; Aznar-Siguan and Bresch, 2019), exposed population (Peduzzi et al., 2012), fatalities (Jonkman, 2005; Formetta and Feyen, 2019), or displacement (IDMC, 2017; Meiler et al., 2025b). Recent studies have also advanced the quantification of indirect and cumulative impacts, including business interruption (Botzen et al., 2019), supply-chain disruption (Verschuur et al., 2020), excess mortality (Young and Hsiang, 2024), migration (Black et al., 2011; Hauer et al., 2020), and long-term economic losses (Hsiang and Jina, 2014). Recovery itself remains less represented in quantitative risk models (Koliou et al., 2020), even though it shapes how long communities remain below function and how initial damage translates into longer-term social and economic disruption.

Methods for recovery modeling are well established, particularly in earthquake engineering (Miles and Chang, 2006). They represent post-disaster rebuilding as the allocation of limited repair resources across damaged buildings, infrastructure systems, or network components (Burton et al., 2016; Blagojević et al., 2023). These models are usually applied at high spatial resolution and for individual events. A recurring result is that the availability of construction resources constrains the pace of recovery (Puri et al., 2024). Evidence from observed disasters and recovery simulations points in the same direction. Johnson and Olshansky (2017) attribute the rapid rebuilding after the 2008 Wenchuan earthquake partly to China's high pre-existing capacity for large-scale urban construction, while an agent-based simulation of about 115,000 buildings in Vancouver found that doubling the available repair workforce substantially shortened housing recovery following an earthquake (Costa et al., 2021).

Applications to climate-related hazards generally take one of two forms. Event-specific studies examine recovery after an individual flood, wildfire, or storm in the affected communities (Birkmann et al., 2023; Friedrich et al., 2024). Broader multi-hazard and compound-event studies represent recovery because the consequences of a subsequent event depend on the time between events and the degree of recovery achieved during that interval. Hurricanes Irma and Maria, which struck Puerto Rico two weeks apart in 2017, are a prominent example (Zscheischler et al., 2018; de Ruiter et al., 2020; Buijs et al., 2026).

At regional scales, climate risk assessments commonly use large synthetic event sets and frequency-weighted metrics, such as expected annual damage and return periods, to examine how changing hazards and exposure affect direct impacts (Aznar-Siguan and Bresch, 2019; Meiler et al., 2022). These metrics identify where the probability and magnitude of damage are greatest, but do not show how the resulting repair demand compares with local capacity. Identifying where high expected impacts coincide with limited construction capacity can inform adaptation planning by showing where efforts to reduce damage may need to be complemented by advance planning for reconstruction support. However, construction capacity remains largely absent from regional probabilistic climate risk assessments.

We address this gap by adding simplified recovery assessments to a building-level probabilistic tropical cyclone (TC) damage model for the US Atlantic and Gulf coasts. Using the open-source climate risk modeling platform CLIMADA (Aznar-Siguan and Bresch, 2019), we estimate housing damage for selected historical events and a large set of synthetic TCs across an inventory of more than 48 million building footprints, representing almost 72 million housing units in 19 US states from Texas to Maine. We then use the estimated housing damage to drive simplified recovery assessments, adapting the demand-versus-capacity logic of the open-source post-disaster recovery model pyrecodes (Blagojević and Stojadinović, 2025). Repair demand represents the physical construction workload generated by damaged housing, while recovery burden compares this workload with local rebuilding capacity. We proxy rebuilding capacity with average monthly residential construction permit activity during a reference period, which we use as a measure of baseline local residential construction activity (Baker et al., 2026). Because permit activity reflects construction-sector activity together with local administrative and market conditions, the recovery burden captures a broader local constraint than physical construction capacity alone and supports relative comparisons across counties and events. This approach allows us to examine when recovery burden is primarily associated with repair demand or limited baseline construction capacity, and where high TC risk coincides with low local capacity.

2 Methods

We estimate building-level TC damage using spatially explicit event-based TC wind footprints (Sect. 2.1.1), a building inventory dataset (Sect. 2.1.2), and impact functions for different structural building types (Cardona et al., 2012) (Fig. 1A), and rescale the resulting structural damage estimates to account for TC rainfall and storm surge-induced damages (Sect. 2.1.3, Fig. 1B). We assign each damaged building to a damage state class and define its repair demand according to that damage severity (Sect. 2.1.4). Finally, we sum each TC's total repair demand per county and report TC damage expressed as the number of weighted units affected (Fig. 1C). We compute the recovery burden resulting from the repair demand, using county-wide construction capacity data (Sect. 2.2.1) to proxy for the county's ability to support residential construction, in a simplified recovery model (Sect. 2.2.2, Fig. 1D).

2.1 Building-level TC damage and repair demand

2.1.1 Hazard data

We use the synthetic TC event set from Gori et al. (2025b), comprising 5,018 synthetic events that represent the 1980–2005 climatology based on NCEP reanalysis and span 1,500 simulation years. The event set provides intensity estimates for three TC hazards: wind, storm surge, and rainfall (Fig. S1). These hazards are modeled with the parametric wind model of Chavas et al. (2015), the ADCIRC hydrodynamic model (Luettich et al., 1992), and the physics-based TC rainfall model TCR (Zhu et al., 2013), respectively. For each event, we use spatially explicit wind fields (m s^{-1}) at a horizontal resolution of 0.1°, reconstructed from the storm track, intensity, and radial size structure. For storm surge and rainfall, the event set provides the maximum storm surge S (m above mean higher high water, MHHW) and total precipitation R (mm) for each county–event pair.

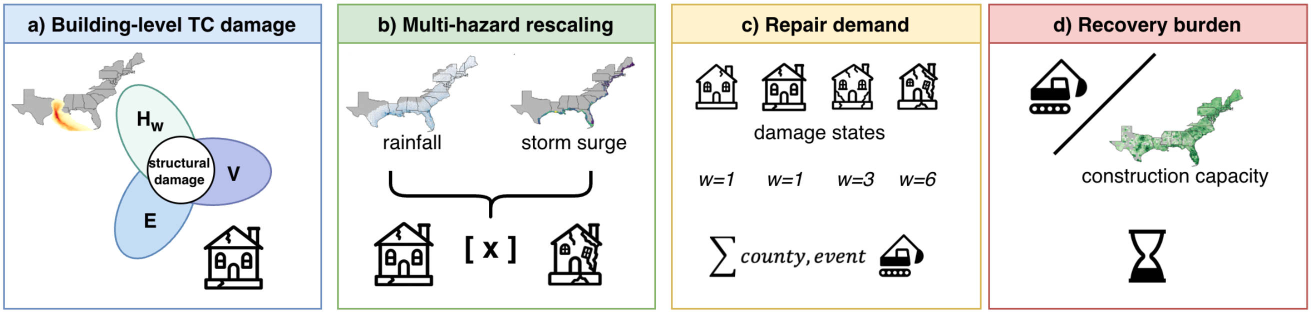

Figure 1. Overview of the TC damage and recovery burden assessment. (a) Spatially explicit TC wind hazard (H_w), building exposure (E), and structural vulnerability represented by impact functions (V) are combined to estimate building-level TC wind damage. (b) County-wide TC rainfall and storm-surge maxima per event are used to rescale the wind-based structural losses, approximating the additional contribution of these hazards to TC damage. (c) Scaled losses are classified into damage states DS1-DS4 and converted to repair demand using relative weights of 1, 1, 3, and 6, respectively. Demand is aggregated for each county-event pair and reported in weighted units affected (WUA). (d) Recovery burden is calculated by comparing repair demand with baseline monthly residential construction capacity, proxied by average residential building permit activity. Recovery burden is reported in capacity-equivalent months of baseline residential construction activity.

For the single-event analyses and comparisons with empirical benchmarks, we additionally use reconstructed wind fields for historical TCs (Gori et al., 2025a). These wind fields combine parametric TC wind estimates with ERA5 surface winds on a 0.05° grid over the Gulf of Mexico, are provided at hourly resolution, and are expressed as 10-m 1-minute sustained winds, consistent with the synthetic event set. We analyze the nine available landfalling TCs that affected our study region: Katrina (2005), Isaac (2012), Hermine (2016), Harvey (2017), Irma (2017), Michael (2018), Laura (2020), Ida (2021), and Ian (2022).

2.1.2 Building inventory

We construct a footprint-level building inventory following the synthesis framework of Lochhead et al. (2026). The inventory combines attributes from several input sources: the National Structure Inventory (NSI); Homeland Infrastructure Foundation-Level Data (HIFLD) for schools, emergency response buildings, and higher education facilities; census block housing-unit counts; and building footprint polygons, which provide the baseline geometry. We use Overture Footprints after comparing footprint sources available across the study region, including USA Structures, OpenStreetMap, and Microsoft Footprints. Our only modification to the national synthesis workflow is the omission of manually generated mobile home park polygons, which were infeasible to create at the scale of the study region.

We use four attributes in downstream simulations: occupancy class, replacement cost, structural type, and number of housing units. Following the national synthesis workflow, occupancy class and replacement cost are derived primarily from the NSI and HIFLD inputs. Structural type is sampled from Hazus-defined relationships between region, occupancy class, design era, and height class. The number of housing units is assigned using the census-based unit-scaling method, which has been shown to approximate detailed local data more closely than NSI-provided unit estimates (Lochhead et al., 2026). The resulting inventory contains 48.6 million building footprints and 71.7 million housing units across 1,193 counties in 19 states along the U.S. Gulf and Atlantic coasts, from Texas to Maine.

2.1.3 Building-level wind damage and multi-hazard scaling

For each event, we calculate building-level wind loss ratios, $L_{e,b}^{\text{wind}}$, representing fractional damage to the building structure. We use the maximum sustained wind speed at every building footprint and TC wind impact functions from the CAPRA platform (Cardona et al., 2012). The impact functions relate wind speed to the expected degree of structural damage for 72 building classes distinguished by construction material and building height. Each building is assigned an impact function based on its structural type. The calculations are performed using the open-source probabilistic climate risk modeling framework CLIMADA (Aznar-Siguan and Bresch, 2019). We set wind loss ratios below 0.5% to zero to exclude negligible impacts.

Explicitly resolving rainfall- and surge-induced flood damage at the building level would require spatially explicit flood depths and corresponding vulnerability functions, which remain computationally demanding for a large event set and study region (Jia and Taflanidis, 2013). We therefore approximate the additional contribution of rainfall and storm surge to total TC damage using the county-level regression model developed by Gori et al. (2025b). For each event–county pair, we select the regression coefficients corresponding to the county's region and coastal or inland classification. We then calculate a multi-hazard scaling factor, $\alpha_{e,c}$, as the ratio of the combined wind, rainfall, and surge regression contributions to the wind contribution alone:

$$\alpha_{e,c} = \max\left(1, \frac{\beta_{\text{wind}} \log(1+W_{e,c}) + \beta_{\text{rain}} \log(1+R_{e,c}) + \beta_{\text{surge}} S_{e,c}}{\beta_{\text{wind}} \log(1+W_{e,c})}\right). \tag{1}$$

Here, $W_{e,c}$, $R_{e,c}$, and $S_{e,c}$ are the county-maximum wind speed, total precipitation, and storm-surge height for event e and county c. The surge contribution is included only for coastal counties. For example, a scaling factor of 1 leaves wind loss unchanged, whereas a value of 1.5 indicates that the combined wind, rainfall, and surge contribution estimated by the regression is 50% larger than the wind contribution alone. The lower bound of 1 prevents rainfall or storm surge from reducing wind-only loss. We set $\alpha_{e,c} = 1$ when the wind contribution is zero or the required regional coefficients are unavailable. For the historical reconstructions, rainfall and storm-surge estimates are available through 2020 only; Hurricane Ida (2021) and Hurricane Ian (2022) are therefore modeled using wind alone.

For every building b in county c, we apply the county-event scaling factor to its building-specific wind loss:

$$L_{e,b} = 1 - \left(1 - L_{e,b}^{\text{wind}}\right)^{\alpha_{e,c}}. \tag{2}$$

where $L_{e,b}$ is the resulting scaled fractional loss. This transformation preserves the spatial variation in building-level wind loss while increasing loss monotonically with $\alpha_{e,c}$ and bounding the result between 0 and 1.

The primary purpose of the rescaling is to represent the potential effect of rainfall and storm surge on damage severity and the resulting repair demand and recovery burden. Available observations do not provide the building-level, hazard-resolved damage data needed to determine whether the scaled losses are more accurate than the wind-only estimates. The relevance of the scaling for the recovery analysis arises from the discrete conversion of fractional losses into damage states: an increase in loss can move housing units into a more severe state and thereby produce a disproportionate increase in repair demand measured in WUA. Compared with the wind-only specification, the scaling increases expected annual repair demand by 10.5%, predominantly through shifts into DS3 and DS4, while leaving county-level rankings and priority classifications largely unchanged (Sect. S7 in the Supplement). Because the same scaling factor is applied throughout a county and only modifies existing wind losses, the approach does not resolve within-county flood patterns or generate damage outside the modeled wind-loss footprint.

2.1.4 Damage state assignment and repair demand

Estimating recovery burden requires information on both the number of damaged housing units and the severity of their damage. We therefore assign each building to a discrete damage state based on its scaled fractional loss, $L_{e,b}$, following the FEMA Hazus TC model (Federal Emergency Management Agency, 2025a): DS0 (none, $L_{e,b} < 0.02$), DS1 (slight, $0.02 \leq L_{e,b} < 0.05$), DS2 (moderate, $0.05 \leq L_{e,b} < 0.10$), DS3 (extensive, $0.10 \leq L_{e,b} < 0.50$), and DS4 (complete, $L_{e,b} \geq 0.50$). Every housing unit within a building inherits the building's damage state. For each event, we count the housing units in each damage state in every county, denoted by $N_{e,c,d}$.

We define repair demand as the physical construction workload generated by damaged housing. It includes repairs to partially damaged units and reconstruction of completely damaged units. To represent differences in workload among damage states, we assign simplified repair times adapted from FEMA Hazus clean-up and repair times for single-family dwellings (Federal Emergency Management Agency, 2024, Table 11-7): 1 month for units in DS1 and DS2, 3 months for units in DS3, and 6 months for units in DS4. We denote these times by τ_d and use their numerical values as relative repair-demand weights, $(w_1, w_2, w_3, w_4) = (1, 1, 3, 6)$.

The repair demand for county c in event e is

$$D_{e,c} = \sum_{d=1}^{4} N_{e,c,d}\, w_d, \tag{3}$$

and is measured in weighted units affected (WUA). A housing unit in DS1 or DS2 contributes 1 WUA, a unit in DS3 contributes 3 WUA, and a unit in DS4 contributes 6 WUA. Units in DS0 do not contribute to repair demand, although their continuous fractional losses remain included in monetary repair cost estimates. Repair demand is the TC damage metric used in the subsequent event-level and probabilistic analyses.

2.2 Recovery burden

2.2.1 Construction capacity data

We proxy local construction capacity, C_c, using residential construction permit activity from the U.S. Census Bureau Building Permits Survey (BPS) (U.S. Census Bureau, 2025). The BPS provides nationally standardized monthly counts of privately owned new residential construction permits by structure type and geography, including counties and Core-Based Statistical Areas (CBSAs) (Baker et al., 2026). We use the average monthly number of housing units authorized across structure types in each county from January through December 2024 as a standardized measure of recent baseline residential construction activity and as the monthly construction capacity in Equation (4). For Connecticut, the BPS reports permits for the nine planning regions that replaced counties as Census county equivalents. To maintain a consistent county geography, we apportion each region's permits among the legacy counties it overlaps according to their shares of housing units. Of the 1,193 counties in the exposure inventory, 753 have non-zero modeled TC repair demand. We calculate recovery burden for the 695 counties that also have positive construction-capacity values; the remaining 58 damage-affected counties are excluded because their 2024 permit activity is either zero or unavailable.

2.2.2 Recovery burden calculation

We calculate recovery burden by comparing the repair demand generated by a TC with the affected county's baseline residential construction capacity. This follows the demand-versus-capacity logic used in pyrecodes, an open-source framework for regional recovery simulation (Blagojević and Stojadinović, 2025). In pyrecodes, recovery is constrained by both the resources available to meet repair demand and the time required to repair damaged components. We represent these two constraints in a simplified county-level calculation without simulating resource allocation over time.

For each damaging event e and county c with positive construction capacity, recovery burden is

$$B_{e,c} = \max\left(\max_{\substack{d\in\{1,2,3,4\} \\ N_{e,c,d}>0}} \tau_d, \frac{D_{e,c}}{C_c} \right), \tag{4}$$

where $D_{e,c}$ is repair demand, C_c is the county's average monthly residential construction capacity, and τ_d is the repair time assigned to damage state d. The first term preserves the minimum repair time implied by the damage states present: even where construction capacity is abundant, the calculation cannot indicate a burden shorter than the longest applicable repair time. The second term represents the repair workload relative to baseline monthly construction capacity.

Relative to wind-only damage, multi-hazard rescaling increases the frequency-weighted sum of county-level recovery burden by 11.8%, compared with a 10.5% increase in total repair demand (Sect. S7).

Recovery burden is expressed in capacity-equivalent months of baseline residential construction activity. For example, a recovery burden of 12 means that the modeled repair workload is equivalent to the amount of new housing the county would normally authorize over 12 months. Higher values indicate greater repair demand relative to baseline local capacity.

Permit activity does not directly measure the construction resources available after a disaster. We use it as an integrated proxy for the local system's ability to support residential construction because it reflects construction-sector activity as well as administrative approval and market and financing conditions. Recovery burden therefore captures a broader potential constraint than physical construction capacity alone, but it still represents only one part of recovery.

The calculation holds construction capacity fixed at its baseline value. In practice, post-disaster capacity may change as local contractors adapt and contractors from outside the affected area enter the affected region (Olsen and Porter, 2011). These dynamics are not represented, and recovery burden should therefore not be interpreted as elapsed recovery duration or as recovery as a whole.

2.3 Probabilistic and event-level summary metrics

We summarize probabilistic TC risk using frequency-weighted annual metrics. Because the synthetic event set spans 1,500 years, each event has an annual occurrence frequency of $1/1500\ \mathrm{yr}^{-1}$. Expected annual repair demand (EARD) is the frequency-weighted sum of repair demand across all events and is expressed in WUA yr^{-1}. We use EARD as our principal measure of TC risk. Expected annual recovery burden (EARB) is calculated analogously and is expressed in capacity-equivalent months per year. Because EARB is an annualized metric, values above 12 indicate a modeled annual burden exceeding one year of baseline construction activity. EARB should be interpreted as an index of recovery burden rather than a measure of recovery time. For the monetary comparison with the FEMA National Risk Index, we also calculate expected annual repair cost (EARC) by multiplying each building's fractional loss by its replacement cost, aggregating the resulting costs by county and event, and applying the same frequency weighting.

To complement the annualized view, we use the same probabilistic event set to examine the consequences of individual damaging TCs. For each county, we consider events that produce non-zero repair demand and calculate the median repair demand and median recovery burden across them. Unlike EARD and EARB, these medians are not annualized; they describe the typical modeled impact when a damaging TC affects the county. The two medians are calculated separately and therefore need not correspond to the same event. We also identify the event producing the greatest repair demand in each county and report its repair demand and corresponding recovery burden in the Sect. S5 in the Supplement.

2.4 Comparison with empirical and index-based benchmarks

We compare selected model outputs with three complementary external benchmarks. None directly observe the quantities at the scales represented by our approach, so the comparisons assess broad spatial consistency and whether relationships have the expected direction rather than providing direct validation. First, county-level damage estimates for historical TCs are compared with FEMA-verified housing damage from OpenFEMA (Federal Emergency Management Agency, 2025b). Second, recovery burden estimates for historical TCs are compared with county-level post-disaster building outcomes reported by Huang et al. (2025). Huang et al. use a vision-language model to compare Google Street View images acquired before and after each event to investigate recovery trajectories. Third, our probabilistic damage estimates, construction-capacity measure, and recovery burden estimates are compared with county-level risk, resilience, and vulnerability metrics from the FEMA National Risk Index (NRI) (Federal Emergency Management Agency, 2023). More detail on the comparison methods, data limitations, and sensitivity analyses is provided in the Sect. S3, S4, and S6 in the Supplement.

3 Results

3.1 Repair demand, construction capacity and recovery burden for Hurricane Laura

Hurricane Laura made landfall in Cameron Parish, Louisiana, on 27 August 2020 as a category 4 storm (Pasch et al., 2021). Our model simulates damage in 20 counties across Louisiana and eastern Texas (Fig. 2b). Calcasieu Parish, which includes Lake Charles and lies close to the landfall region, has the largest modeled repair demand, with 43,859 WUA, more than one-third of the storm total. However, it ranks near the middle of the affected counties in recovery burden (Table S1).

The spatial differences between repair demand and recovery burden show why damage alone is insufficient to characterize recovery conditions. Once repair demand is evaluated relative to local construction capacity, counties with similar repair demands can have very different recovery burdens, while counties with different repair demands can have similar burdens. Rapides and Vernon parishes have similar repair demands, with 7,561 and 7,168 WUA, respectively (Fig. 2b), but their recovery burdens differ by nearly an order of magnitude (Fig. 2d) because their construction capacities (Fig. 2c) differ strongly (Table S1). Conversely, Calcasieu has 5.8 times the repair demand of Rapides but also substantially greater construction capacity, resulting in similar recovery burdens. The largest recovery burdens occur where high repair demand coincides with limited construction capacity. Beauregard Parish, for example, has the second-largest repair demand, with 19,746 WUA, but a baseline construction capacity of only 6.9 housing units authorized per month, resulting in one of the largest recovery burdens. Recovery burden is therefore shaped jointly by the damage caused by the storm and the local capacity to rebuild.

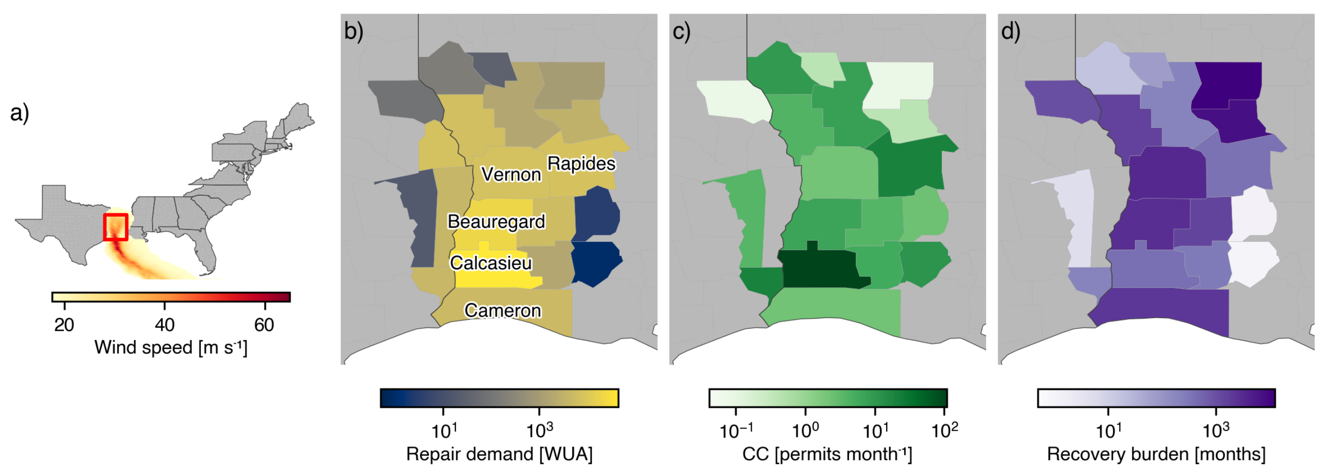

Figure 2. Repair demand and recovery burden for Hurricane Laura (2020). (a) Maximum sustained wind speed (m s^{-1}), with the red box marking the focus region shown in the remaining panels; (b) repair demand, $D_{e,c}$, measured in weighted units affected (WUA); (c) construction capacity, C_c (CC; residential permits month^{-1}); and (d) recovery burden, $B_{e,c}$, expressed in months of baseline construction activity. The Louisiana parishes labeled in panel (b) are Cameron, Calcasieu, Beauregard, Vernon, and Rapides. Higher recovery burden indicates greater repair demand relative to baseline construction capacity.

3.2 Evaluation against observed damage and recovery for historical TCs

We next evaluate whether the modeled damage and recovery burden are consistent with observations across historical TCs. For damage, the primary observational reference is FEMA-verified real property damage from Individual Assistance records (Sect. 2.4). We evaluate whether the model captures both the spatial damage footprint and differences in damage severity among counties. Footprint detection, defined as the percentage of total FEMA-verified damage across all declared counties that falls in counties with non-zero modeled damage, is high for hurricanes Michael (2018), Laura (2020), Ida (2021), and Ian (2022), at 99%, 92%, 96%, and 82%, respectively. To compare county-level damage patterns across storms of different sizes, we express the damage in each matched county as a share of the total damage across all matched counties for that storm. We calculate these shares separately for modeled repair demand and FEMA-verified damage and then pool the county–storm observations across all historical TCs. The modeled and verified damage shares are moderately correlated across the pooled observations ($r_s = +0.56$, $p < 0.001$, $n = 96$; Table S2). The storm-specific correlations generally remain similar or increase after both quantities are divided by residential exposure units, suggesting that the agreement is not driven primarily by differences in county size (Table S3).

The comparison also shows the limitations of a damage model in which spatial damage patterns are derived from wind footprints and rainfall and storm surge are represented through county-level scaling (Sect. 2.1.3). For Katrina (2005), footprint detection is high but the county ranking is weak: 95% of FEMA-verified damage falls in counties with non-zero modeled damage, but the rank correlation across matched counties is only $r_s = +0.34$ ($p = 0.192$, $n = 16$; Table S2). This pattern is consistent with the importance of storm surge and levee-failure losses within the affected region. Harvey (2017) shows the opposite pattern. The county ranking is strong within the modeled damage footprint ($r_s = +0.80$, $p = 0.010$, $n = 9$), but the footprint captures only 4% of FEMA-verified damage because much of the observed damage was caused by freshwater flooding outside the modeled footprint. These cases illustrate limitations of the damage model rather than of the recovery-burden calculation.

Observed recovery outcomes from Huang et al. (2025) provide a first-order check on the recovery-burden component. Across matched county–storm observations with at least ten assessed buildings with visible changes, construction capacity is positively associated with the observed rebuild rate ($r_s = +0.52$, $p = 0.033$, $n = 17$; Table S4). Modeled recovery burden is negatively associated with the observed recovery score, as anticipated ($r_s = -0.41$, $p = 0.10$, $n = 17$). Given the small number of observations, these associations should be interpreted cautiously. Nevertheless, both have the expected direction where greater construction capacity is associated with a higher observed rebuild rate, while greater modeled recovery burden is associated with a lower observed recovery score. Taken together, the historical comparisons provide initial support for using the model for relative spatial comparisons of repair demand and recovery burden.

3.3 Probabilistic perspective on recovery burden

We evaluate recovery burden across the full probabilistic TC event set from two perspectives: as an expected annual quantity, following standard probabilistic risk assessment, and through county-level event summaries of the damaging storms affecting each county (Sect. 2.3).

TC risk, measured as expected annual repair demand (EARD; Fig. 3a), is concentrated along the Gulf Coast and in South Florida, where frequent TC exposure coincides with dense coastal housing. Construction capacity (CC; Fig. 3b) follows a different spatial pattern. It is highest in large metropolitan counties and varies by more than four orders of magnitude across the study counties, from approximately 0.08 to 2,490 residential permits per month. Expected annual recovery burden (EARB; Fig. 3c) follows the geography of EARD more closely than that of construction capacity. Counties with the largest expected annual repair demand therefore also tend to have the greatest expected annual recovery burden, particularly along the Gulf Coast and in South Florida.

This visual pattern is confirmed by the driver analysis in Fig. 4. EARB is strongly associated with EARD (Spearman $r_s = +0.78$; Fig. 4a) and moderately negatively associated with construction capacity ($r_s = -0.48$; Fig. 4b). Annual aggregation emphasizes the upper tail of the event distribution. Event-level repair-demand distributions are strongly right-skewed in most counties (Fig. S3), so a small number of high-impact storms contribute disproportionately to expected annual values. For these tail events, the modeled repair workload can exceed one month of baseline construction activity by orders of magnitude. Differences in repair demand therefore outweigh differences in construction capacity, and EARB primarily mirrors the probabilistic damage metric. The same pattern appears for each county's maximum-repair-demand event (Fig. S4), for which recovery burden is again governed primarily by repair-demand magnitude (Spearman $r_s = +0.65$; Fig. S5).

The county-level medians across damaging events give a different result (Fig. S6). Median recovery burden is less strongly associated with median repair demand ($r_s = +0.38$; Fig. 4c) and more strongly negatively associated with construction capacity ($r_s = -0.73$; Fig. 4d). In this part of the event distribution, repair demand is smaller relative to local monthly construction activity. Construction capacity therefore becomes the main differentiator among counties facing comparable repair demands.

3.4 Screening for potential post-disaster construction bottlenecks

TC risk and baseline construction capacity are distinct county properties that jointly shape recovery burden. We combine these two factors in a first-order screen to identify counties where high expected repair demand coincides with limited local construction capacity. Such counties may require rapid post-disaster mobilization of external construction workers, building materials, and other reconstruction support. We rank the 695 counties with non-zero modeled TC repair demand and positive construction capacity data into terciles of expected annual repair demand (EARD), the measure of TC risk, and construction capacity (CC). The terciles are defined across all 695 counties included in the analysis and combined into nine risk–capacity classes (Fig. 5).

The highest-risk tercile contains 95 counties that also fall in the highest-capacity tercile. These are mostly large metropolitan coastal counties, including Harris (Texas), Miami-Dade (Florida), and Hillsborough (Florida). Although major events will

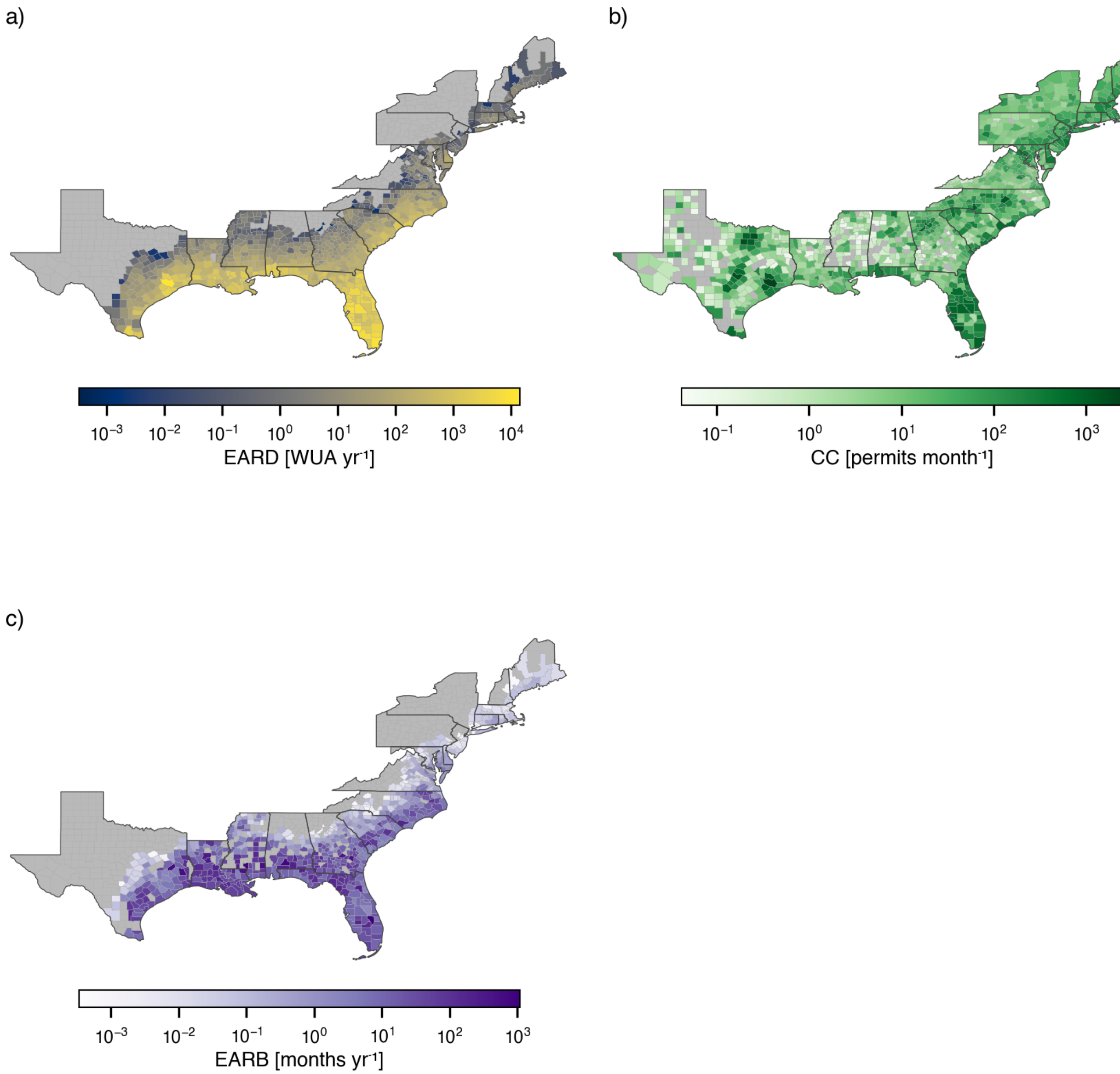

Figure 3. Geography of annual TC risk and recovery burden. (a) Expected annual repair demand (EARD; WUA yr^{-1}), (b) construction capacity, C_c (CC; residential permits month^{-1}), and (c) expected annual recovery burden (EARB; capacity-equivalent months yr^{-1}) across the US Atlantic and Gulf coasts. Gray denotes counties with zero or unavailable values for the corresponding metric.

produce widespread damage, these counties have high baseline construction capacity compared with other counties across the study area; their primary challenge is therefore high repair demand rather than unusually limited local capacity. In contrast, 60 counties in the highest-risk tercile fall into the lowest-capacity tercile. These high-risk, low-capacity counties are concentrated

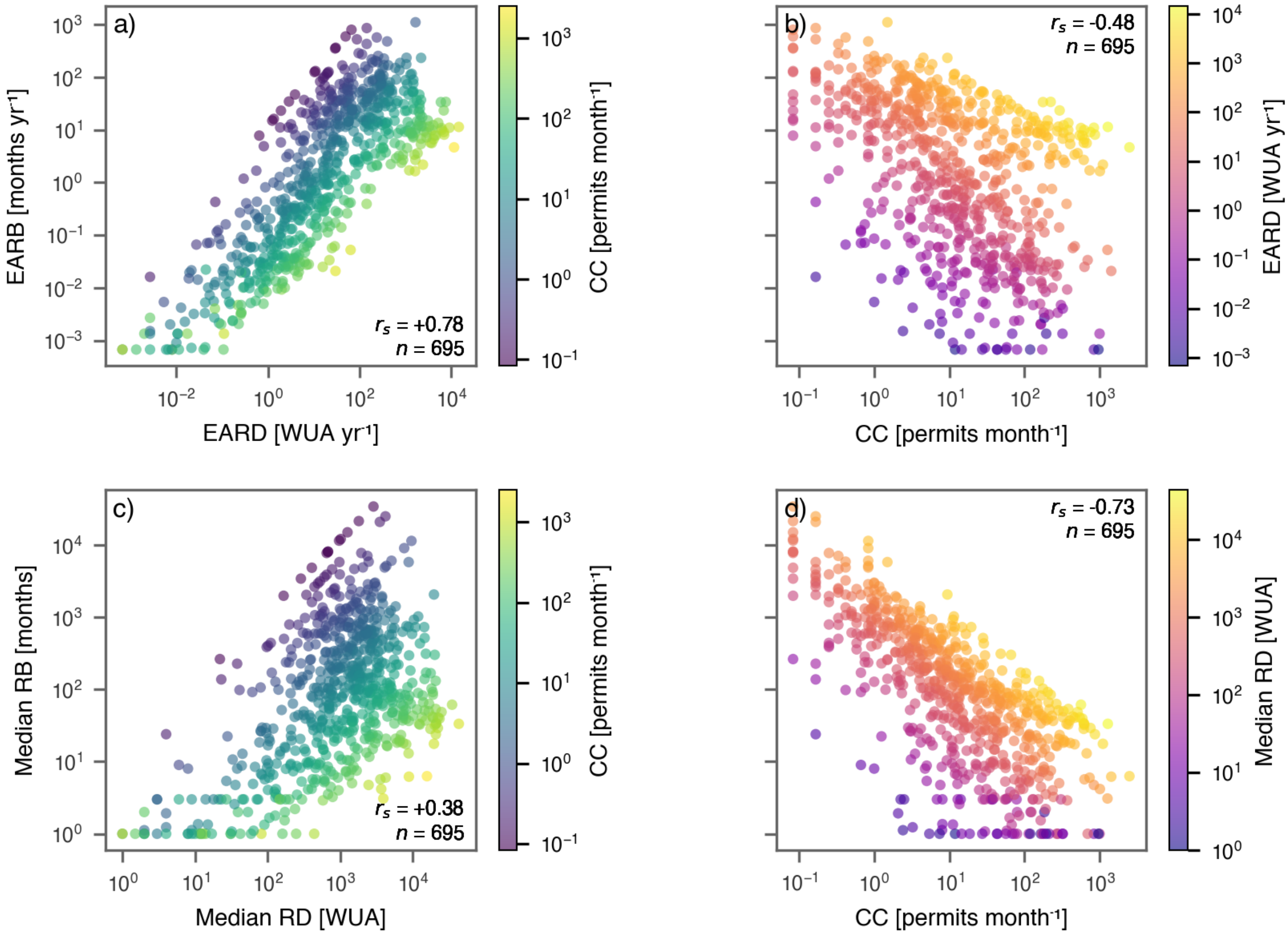

Figure 4. Drivers of recovery burden under annual and county-level per-event perspectives. (a) Expected annual recovery burden (EARB) versus expected annual repair demand (EARD); (b) EARB versus construction capacity (CC); (c) median damaging event recovery burden (RB) versus median repair demand (RD); and (d) median damaging event recovery burden versus construction capacity. Median metrics are calculated separately for each county and therefore need not correspond to the same TC across counties. Spearman rank correlations (r_s) and the number of counties with available data (n) are shown in each panel.

along the Gulf Coast, in Louisiana (13 counties), Mississippi (7), Alabama (5), and Texas (7), and along the South Atlantic coast, in Georgia (13), Florida (10), and the Carolinas (5). They are predominantly smaller, less urban counties. Their construction capacity ranges from 0.17 to 4.6 residential permits per month, with a median of 2.5, compared with a median of approximately 12 permits per month across all 695 counties included in the analysis. The screen therefore identifies these counties as particularly susceptible to local post-disaster construction bottlenecks and potentially requiring additional external support following a major TC.

Counties with medium to low TC risk and low construction capacity form a different group. They are mainly located farther inland and outside urban centers, including counties in Georgia, Mississippi, Texas, and Alabama. Although their expected annual repair demand is lower, their limited baseline capacity means that they may still face such bottlenecks when a damaging event occurs. Finally, counties with moderate to high construction capacity and medium to low TC risk do not stand out as potential capacity-constrained locations under present-day conditions. These counties are mostly located in the Mid-Atlantic and Northeast and in inland metropolitan regions such as those around San Antonio and Austin. Their classification may nevertheless change if TC hazards shift with climate change (Knutson et al., 2020) or exposure increases through coastal and inland development.

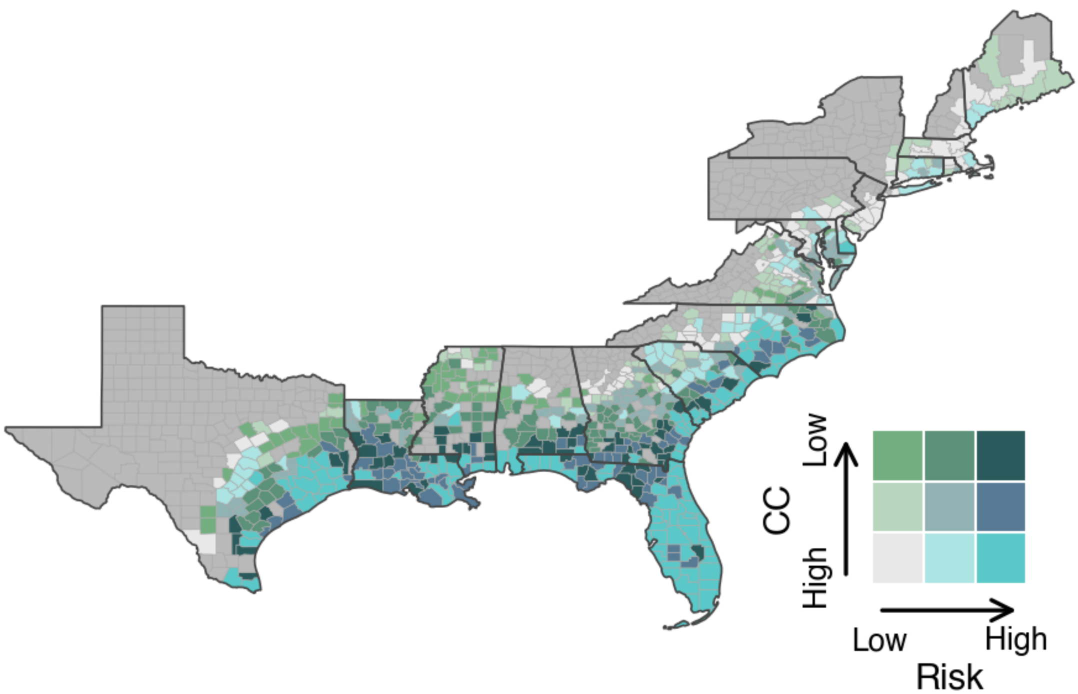

Figure 5. Screening for potential post-disaster construction bottlenecks. Counties are classified by terciles of expected annual repair demand (EARD), as a measure of TC risk, and baseline construction capacity (CC) across the 695 study counties with non-zero modeled TC damage and positive construction-capacity data. Counties not meeting these criteria are shown in gray.

3.5 Comparison with FEMA NRI risk, resilience, and vulnerability metrics

We compare the probabilistic results with related county-level metrics from the FEMA National Risk Index (NRI) (Federal Emergency Management Agency, 2023). The NRI expected annual loss provides an external reference for the spatial distribution of probabilistic damage, while its Community Resilience and Social Vulnerability scores provide broader context for construction capacity and recovery burden. Modeled expected annual repair costs rank counties similarly to the NRI hurricane expected annual loss, with Spearman correlations of 0.63–0.65 (Table S5), indicating broad spatial agreement between the probabilistic damage estimates. Construction capacity is higher in counties with greater Community Resilience ($r_s = +0.42$) and lower Social Vulnerability ($r_s = -0.63$). Conversely, median damaging-event recovery burden is higher in counties with lower Community Resilience ($r_s = -0.44$) and greater Social Vulnerability ($r_s = +0.56$). The association between median recovery burden and Social Vulnerability remains essentially unchanged after controlling for exposure using either modeled expected annual repair demand or NRI hurricane expected annual loss (Table S5). These relationships show that the spatial patterns of construction capacity and recovery burden are consistent with broader dimensions of community resilience and vulnerability.

The comparison also shows that the risk–capacity screening does not fully overlap with the NRI indices. Of the 60 high-risk, low-capacity counties, 35 fall in the highest Social Vulnerability tercile and 37 in the lowest Community Resilience tercile. These groups overlap, and 12 counties fall into neither group (Table S6). Explicitly representing baseline construction capacity therefore identifies potential reconstruction constraints that are not fully captured by the broader socioeconomic indicators included in the NRI.

4 Discussion

In this study, we combine methods of probabilistic climate risk modeling with post-disaster recovery simulations at a broad regional scale. We learn that the perspective from which we evaluate the resulting recovery burden matters for its interpretation. Seen through the lens of annualized risk metrics, recovery burden is highest in areas of high TC risk. When approached from an event perspective, which is common in post-disaster recovery modeling, the local construction capacity is more informative for recovery burden. Moreover, we learn that contextualizing US tropical cyclone risk through the joint representation of damage and construction capacity allows us to identify priority counties that may be particularly susceptible to post-disaster construction bottlenecks. That is, low baseline capacity indicates where regional mutual-aid agreements, advance coordination with contractors, and plans for rapidly mobilizing workers and building materials may be most important after a major TC. High-risk counties with high baseline capacity may also require external support after extreme events, but within our model, limited local construction capacity is less likely to be their main constraint.

Several simplifications bound this interpretation. The damage model uses spatially explicit wind fields, while rainfall and storm surge are represented through county-level scaling of wind-based damage (Sect. 2.1.3). The recovery assessment is based on residential permits data that represent baseline construction activity rather than surge capacity that may be available after a disaster (Baker et al., 2026) and the model holds capacity fixed at the county scale (Johnson and Olshansky, 2017; Costa et al., 2021) (Sect. 2.2). Construction capacity coverage may also affect the identification of counties with potential post-disaster construction bottlenecks. Nine of the 58 damage-affected counties excluded because no positive construction-capacity estimate was available exceed the threshold for the highest EARD tercile, so the screening may omit additional high-risk, low-capacity counties (Sect. 3.4). The comparison with external benchmarks generally corresponds with observed TC damage footprints and severity; the expected direction of association with observed recovery results (Sect. 3.2); and broad consistency with the FEMA NRI Community Resilience and Social Vulnerability indices (Sect. 3.5). However, it also highlights that the available data for evaluation is very sparse and limited for a broad regional recovery evaluation. Notably, previous studies have found that the empirical performance of composite vulnerability and resilience indices varies across disaster outcomes (Cutter et al., 2014; Bakkensen et al., 2017).

The most important next step is to connect relative recovery burden with observed recovery processes. Emerging datasets provide several possible starting points, including building-level recovery trajectories from repeated Street View imagery (Huang et al., 2025), permit-based reconstruction records (Baker et al., 2026), and satellite observations of post-disaster change (Friedrich et al., 2024). None of these sources covers recovery completely, but they constrain different parts of the process, and a recovery model calibrated against them could turn recovery burden into an estimate of recovery duration with quantified uncertainty. Construction capacity itself also deserves closer study. Our county-level approach does not represent how repair resources are drawn from neighboring counties and beyond, so a natural refinement is to represent capacity as a regional pool with distance- or market-based allocation, informed by observed post-disaster labor and contractor flows (Costa et al., 2021). Such a model could distinguish counties with limited local capacity but strong access to regional construction markets from those that are remote from these resources.

Our approach is not specific to TCs. Any hazard model that produces housing damage states can drive the recovery assessment, allowing the approach to extend to flooding, wildfires, and earthquakes, as well as multi-hazard settings in which the same construction capacity must absorb repair demands from successive events (de Ruiter et al., 2020; Zscheischler et al., 2018). Because the event set represents the 1980–2005 climatology (Gori et al., 2025b), applying the model to future TC climatologies and corresponding scenarios of exposure and construction capacity would show how the joint geography of risk and capacity may shift under climate and socioeconomic change (Meiler et al., 2025a). Recovery also connects risk assessment with adaptation because reconstruction is one of the few moments when the building stock changes quickly. Extending the recovery assessments to include rebuilding to higher standards or in safer locations (UNISDR, 2015) would allow the effects of recovery decisions on future damage to be represented explicitly.

5 Conclusions

Probabilistic climate risk assessment commonly ends with estimates of direct damage. We extend this assessment by comparing building-level residential repair demand with baseline county construction capacity across the US Atlantic and Gulf coasts. Expected annual recovery burden largely follows expected annual repair demand because rare, high-impact events contribute disproportionately to annualized values. For the median damaging event, construction capacity is more strongly associated with recovery burden, and counties with comparable repair demand can face substantially different burdens.

A joint screen identifies 60 high-risk, low-capacity counties, concentrated in smaller, less urban counties along the Gulf and South Atlantic coasts. This screen provides a first-order indication of potential construction bottlenecks, rather than an estimate of recovery duration. Considering TC risk and construction capacity together can show where advance planning for reconstruction support may complement measures to reduce physical damage. Testing these patterns against observed recovery and representing regional flows of construction resources are important next steps.

Code and data availability. The building inventory and the spatially explicit tropical cyclone wind footprints used in this study, for both the synthetic event set and the nine historical storms, are openly available at the NSF DesignSafe-CI https://doi.org/10.17603/ds2-hy5r-y437 (Meiler et al., 2026).

The county-wide storm surge and rainfall maxima that were used for the multi-hazard damage scaling (Gori et al., 2025b) are openly available at the NSF DesignSafe-CI https://doi.org/10.17603/ds2-0jkm-h487.

Intermediate and output data are not archived separately, as they can be regenerated from these inputs using the code below. Code to reproduce the results of this paper is available at a GitHub repository (Meiler and Blagojevic, 2026) with the identifier 10.5281/zenodo.22086702.

Author contributions. SM: Conceptualization, Data curation, Formal analysis, Funding acquisition, Investigation, Methodology, Project administration, Software, Visualization, Writing – original draft, Writing – review & editing; NB: Conceptualization, Methodology, Software, Writing – review & editing; ML: Data Curation, Resources, Writing – review & editing; AG: Resources, Writing – review & editing; JWB: Funding acquisition, Supervision, Writing – review & editing

Competing interests. The authors declare that they have no competing interests.

Acknowledgements. SM acknowledges support from the Swiss National Science Foundation Postdoc.Mobility Fellowship (P500PN_222189) and from the Stanford Urban Resilience Initiative. ML acknowledges funding from the National Science Foundation Graduate Research Fellowship Program and Stanford Graduate Fellowship.

References

Aznar-Siguan, G. and Bresch, D. N.: CLIMADA v1: A global weather and climate risk assessment platform, Geoscientific Model Development, 12, 3085–3097, https://doi.org/10.5194/gmd-12-3085-2019, 2019.

Baker, J., Blagojevic, N., and Zhang, S.: Single-Family Residential Reconstruction after Disasters: Building Permits Survey Data and Synthetic Controls, https://doi.org/10.31224/6637, preprint, Engineering Archive, 2026.

Bakkensen, L. A., Fox-Lent, C., Read, L. K., and Linkov, I.: Validating Resilience and Vulnerability Indices in the Context of Natural Disasters, Risk Analysis, 37, 982–1004, https://doi.org/10.1111/risa.12677, 2017.

Birkmann, J., Schüttrumpf, H., Handmer, J., Thieken, A., Kuhlicke, C., Truedinger, A., Sauter, H., Klopries, E.-M., Greiving, S., Jamshed, A., Merz, B., Solecki, W., and Kirschbauer, L.: Strengthening Resilience in Reconstruction after Extreme Events – Insights from Flood Affected Communities in Germany, International Journal of Disaster Risk Reduction, 96, 103 965, https://doi.org/10.1016/j.ijdrr.2023.103965, 2023.

Black, R., Adger, W. N., Arnell, N. W., Dercon, S., Geddes, A., and Thomas, D.: The effect of environmental change on human migration, Global Environmental Change, 21, S3–S11, https://doi.org/10.1016/j.gloenvcha.2011.10.001, 2011.

Blagojević, N., Hefti, F., Henken, J., Didier, M., and Stojadinović, B.: Quantifying Disaster Resilience of a Community with Interdependent Civil Infrastructure Systems, Structure and Infrastructure Engineering, 19, 1696–1710, https://doi.org/10.1080/15732479.2022.2052912, 2023.

Blagojević, N. and Stojadinović, B.: pyrecodes: an open-source library for regional recovery simulation and disaster resilience assessment of the built environment (v0.2.0), https://doi.org/10.5281/zenodo.14774265, 2025.

Botzen, W. J. W., Deschenes, O., and Sanders, M.: The Economic Impacts of Natural Disasters: A Review of Models and Empirical Studies, Review of Environmental Economics and Policy, 13, 167–188, https://doi.org/10.1093/reep/rez004, 2019.

Bruneau, M., Chang, S. E., Eguchi, R. T., Lee, G. C., O'Rourke, T. D., Reinhorn, A. M., Shinozuka, M., Tierney, K., Wallace, W. A., and von Winterfeldt, D.: A Framework to Quantitatively Assess and Enhance the Seismic Resilience of Communities, Earthquake Spectra, 19, 733–752, https://doi.org/10.1193/1.1623497, 2003.

Buijs, S. L., Sauer, I. J., Kropf, C. M., Juhel, S., Stalhandske, Z., Claassen, J. N., and De Ruiter, M. C.: Exploring recovery complexity in the context of consecutive disasters, Natural Hazards and Earth System Sciences, 26, 3559–3578, https://doi.org/10.5194/nhess-26-3559-2026, 2026.

Burton, H. V., Deierlein, G., Lallemant, D., and Lin, T.: Framework for Incorporating Probabilistic Building Performance in the Assessment of Community Seismic Resilience, Journal of Structural Engineering, 142, C4015 007, https://doi.org/10.1061/(ASCE)ST.1943-541X.0001321, 2016.

Cardona, O.-D., van Aalst, M. K., Birkmann, J., Fordham, M., McGregor, G., Perez, R., Pulwarty, R. S., Schipper, E. L. F., Sinh, B. T., Décamps, H., Keim, M., Davis, I., Ebi, K. L., Lavell, A., Mechler, R., Murray, V., Pelling, M., Pohl, J., Smith, A.-O., and Thomalla, F.: Determinants of Risk: Exposure and Vulnerability, in: Managing the Risks of Extreme Events and Disasters to Advance Climate Change Adaptation, edited by Field, C. B., Barros, V., Stocker, T. F., and Dahe, Q., vol. 9781107025, pp. 65–108, Cambridge University Press, Cambridge, ISBN 978-1-139-17724-5, https://doi.org/10.1017/CBO9781139177245.005, 2012.

Chavas, D. R., Lin, N., and Emanuel, K.: A model for the complete radial structure of the tropical cyclone wind field. Part I: Comparison with observed structure, Journal of the Atmospheric Sciences, 72, 3647–3662, https://doi.org/10.1175/JAS-D-15-0014.1, 2015.

Costa, R., Haukaas, T., and Chang, S. E.: Agent-Based Model for Post-Earthquake Housing Recovery, Earthquake Spectra, 37, 46–72, https://doi.org/10.1177/8755293020944175, 2021.

Cutter, S. L., Barnes, L., Berry, M., Burton, C., Evans, E., Tate, E., and Webb, J.: A Place-Based Model for Understanding Community Resilience to Natural Disasters, Global Environmental Change, 18, 598–606, https://doi.org/10.1016/j.gloenvcha.2008.07.013, 2008.

Cutter, S. L., Ash, K. D., and Emrich, C. T.: The Geographies of Community Disaster Resilience, Global Environmental Change, 29, 65–77, https://doi.org/10.1016/j.gloenvcha.2014.08.005, 2014.

de Ruiter, M. C., Couasnon, A., van den Homberg, M. J., Daniell, J. E., Gill, J. C., and Ward, P. J.: Why We Can No Longer Ignore Consecutive Disasters, Earth's Future, 8, https://doi.org/10.1029/2019EF001425, 2020.

Din, A.: What Do Visualizations of Administrative Address Data Show About the Camp Fire in Paradise, California?, Cityscape, 24, https://www.huduser.gov/portal/periodicals/cityscape/vol24num3/article10.html, 2022.

Federal Emergency Management Agency: National Risk Index Technical Documentation, Tech. rep., U.S. Department of Homeland Security, Federal Emergency Management Agency, Washington, DC, https://www.fema.gov/sites/default/files/documents/fema_national-risk-index_technical-documentation.pdf, 2023.

Federal Emergency Management Agency: Hazus Earthquake Model Technical Manual, Hazus 6.1, Tech. Rep., Federal Emergency Management Agency, https://www.fema.gov/sites/default/files/documents/fema_hazus-earthquake-model-technical-manual-6-1.pdf, 2024.

Federal Emergency Management Agency: Hazus 7.0 Hurricane Model Technical Manual, Tech. rep., Federal Emergency Management Agency, Washington, DC, https://www.fema.gov/flood-maps/tools-resources/flood-map-products/hazus/documentation, 2025a.

Federal Emergency Management Agency: OpenFEMA Dataset: Housing Assistance Program Data – Owners – V2, https://www.fema.gov/openfema-data-page/housing-assistance-program-data-owners-v2, 2025b.

Formetta, G. and Feyen, L.: Empirical Evidence of Declining Global Vulnerability to Climate-Related Hazards, Global Environmental Change, 57, 101 920, https://doi.org/10.1016/j.gloenvcha.2019.05.004, 2019.

Friedrich, H. K., Tellman, B., Sullivan, J. A., Saunders, A., Zuniga-Teran, A. A., Bakkensen, L. A., Cawley, M., Dolk, M., Emberson, R. A., Forrest, S. A., Gupta, N., Gyawali, N., Hall, C. A., Kettner, A. J., Lozano, J. L. S., and Bola, G. B.: Earth Observation to Address Inequities in Post-Flood Recovery, Earth's Future, 12, e2023EF003 606, https://doi.org/10.1029/2023EF003606, 2024.

Gori, A., Hasan, F., and Weng, Y.: Reconstructions of Hurricane Storm Tides Along the US Coastline From 1940 to Present, in: AGU Fall Meeting 2025, AGU, https://studio.m-anage.com/agu/agu25/meetingapp.cgi/Paper/1895497, 2025a.

Gori, A., Lin, N., Chavas, D., Oppenheimer, M., and Xian, S.: Sensitivity of Tropical Cyclone Risk across the US to Changes in Storm Climatology and Socioeconomic Growth, Environmental Research Letters, 20, 064 050, https://doi.org/10.1088/1748-9326/add60d, 2025b.

Hauer, M. E., Fussell, E., Mueller, V., Burkett, M., Call, M., Abel, K., McLeman, R., and Wrathall, D.: Sea-level rise and human migration, Nature Reviews Earth & Environment, 1, 28–39, https://doi.org/10.1038/s43017-019-0002-9, 2020.

Hsiang, S. and Jina, A.: The Causal Effect of Environmental Catastrophe on Long-Run Economic Growth: Evidence From 6,700 Cyclones, Tech. Rep. w20352, National Bureau of Economic Research, Cambridge, MA, https://doi.org/10.3386/w20352, 2014.

Huang, T., Zanocco, C., Wang, Z., Hwang, J., and Rajagopal, R.: Built Environment Disparities Are Amplified during Extreme Weather Recovery, Nature, 648, 349–356, https://doi.org/10.1038/s41586-025-09804-3, 2025.

IDMC: Global disaster displacement risk: a baseline for future work, Tech. rep., Internal Displacement Monitoring Centre (IDMC), https://www.internal-displacement.org/publications/global-disaster-displacement-risk-a-baseline-for-future-work, 2017.

Jia, G. and Taflanidis, A. A.: Kriging Metamodeling for Approximation of High-Dimensional Wave and Surge Responses in Real-Time Storm/Hurricane Risk Assessment, Computer Methods in Applied Mechanics and Engineering, 261–262, 24–38, https://doi.org/10.1016/j.cma.2013.03.012, 2013.

Johnson, L. A. and Olshansky, R. B.: After Great Disasters: How Six Countries Managed Community Recovery, Lincoln Institute of Land Policy, ISBN 978-1-55844-331-0, 2017.

Jonkman, S. N.: Global Perspectives on Loss of Human Life Caused by Floods, Natural Hazards, 34, 151–175, https://doi.org/10.1007/s11069-004-8891-3, 2005.

Knapp, E. E., Valachovic, Y. S., Quarles, S. L., and Johnson, N. G.: Housing Arrangement and Vegetation Factors Associated with Single-Family Home Survival in the 2018 Camp Fire, California, Fire Ecology, 17, 25, https://doi.org/10.1186/s42408-021-00117-0, 2021.

Knutson, T., Camargo, S. J., Chan, J. C., Emanuel, K., Ho, C. H., Kossin, J., Mohapatra, M., Satoh, M., Sugi, M., Walsh, K., and Wu, L.: Tropical cyclones and climate change assessment part II: Projected response to anthropogenic warming, Bulletin of the American Meteorological Society, 101, E303–E322, https://doi.org/10.1175/BAMS-D-18-0194.1, 2020.

Koliou, M., van de Lindt, J. W., McAllister, T. P., Ellingwood, B. R., Dillard, M., and Cutler, H.: State of the Research in Community Resilience: Progress and Challenges, Sustainable and Resilient Infrastructure, 5, 131–151, https://doi.org/10.1080/23789689.2017.1418547, 2020.

Lochhead, M., Zsarnoczay, A., and Deierlein, G. G.: Exposure Matters: A Synthesis Framework for High-Resolution Building Inventory Development, International Journal of Disaster Risk Reduction, 139, 106 148, https://doi.org/10.1016/j.ijdrr.2026.106148, 2026.

Luettich, R. A., Westerink, J. J., and Scheffner, N. W.: ADCIRC: An Advanced Three-Dimensional Circulation Model for Shelves, Coasts, and Estuaries. Report 1: Theory and Methodology of ADCIRC-2DDI and ADCIRC-3DL, Dredging Research Program Technical Report DRP-92-6, Coastal Engineering Research Center, U.S. Army Corps of Engineers, Vicksburg, MS, 1992.

Markhvida, M., Walsh, B., Hallegatte, S., and Baker, J.: Quantification of Disaster Impacts through Household Well-Being Losses, Nature Sustainability, 3, 538–547, https://doi.org/10.1038/s41893-020-0508-7, 2020.

Meiler, S. and Blagojevic, N.: simonameiler/hurricane_recovery_potential: v1.0.0, https://doi.org/10.5281/zenodo.22086702, 2026.

Meiler, S., Vogt, T., Bloemendaal, N., Ciullo, A., Lee, C.-Y., Camargo, S. J., Emanuel, K., and Bresch, D. N.: Intercomparison of regional loss estimates from global synthetic tropical cyclone models, Nature Communications, 13, 6156, https://doi.org/10.1038/s41467-022-33918-1, 2022.

Meiler, S., Kropf, C. M., McCaughey, J. W., Lee, C.-Y., Camargo, S. J., Sobel, A. H., Bloemendaal, N., Emanuel, K., and Bresch, D. N.: Navigating and attributing uncertainty in future tropical cyclone risk estimates, Science Advances, 11, eadn4607, https://doi.org/10.1126/sciadv.adn4607, 2025a.

Meiler, S., Mühlhofer, E., Lüthi, S., Bresch, D. N., Ottonelli, D., Ghizzoni, T., Trasforini, E., Rudari, R., Rossi, L., Kasmalkar, I., Mohammadiamanab, N., Daou, D., Nguyen, T.-L., Gyawali, D. R., Peter, M., Oakes, R., Souvignet, M., and Ponserre, S.: A natural hazard risk modelling approach to human displacement - frontiers & challenges, Environmental Research: Climate, 4, 045 001, https://doi.org/10.1088/2752-5295/ae014c, 2025b.

Meiler, S., Lochhead, M., and Gori, A.: Residential building inventory and tropical cyclone wind hazard footprints for United States Atlantic and Gulf Coast counties, https://doi.org/10.17603/ds2-hy5r-y437, project PRJ-6475, 2026.

Miles, S. B. and Chang, S. E.: Modeling Community Recovery from Earthquakes, Earthquake Spectra, 22, 439–458, https://doi.org/10.1193/1.2192847, 2006.

Olsen, A. H. and Porter, K. A.: What We Know about Demand Surge: Brief Summary, Natural Hazards Review, 12, 62–71, https://doi.org/10.1061/(ASCE)NH.1527-6996.0000028, 2011.

Pasch, R. J., Berg, R., Roberts, D. P., and Papin, P. P.: Tropical Cyclone Report: Hurricane Laura (AL132020), 20–29 August 2020, Tech. rep., National Hurricane Center, Miami, FL, https://www.nhc.noaa.gov/data/tcr/AL132020_Laura.pdf, 2021.

Peduzzi, P., Chatenoux, B., Dao, H., De Bono, A., Herold, C., Kossin, J., Mouton, F., and Nordbeck, O.: Global trends in tropical cyclone risk, Nature Climate Change, 2, 289–294, https://doi.org/10.1038/nclimate1410, 2012.

Puri, A., Elkharboutly, M., and Ali, N. A.: Identifying Major Challenges in Managing Post-Disaster Reconstruction Projects: A Critical Analysis, International Journal of Disaster Risk Reduction, 107, 104 491, https://doi.org/10.1016/j.ijdrr.2024.104491, 2024.

Román, M. O., Stokes, E. C., Shrestha, R., Wang, Z., Schultz, L., Carlo, E. A. S., Sun, Q., Bell, J., Molthan, A., Kalb, V., Ji, C., Seto, K. C., McClain, S. N., and Enenkel, M.: Satellite-Based Assessment of Electricity Restoration Efforts in Puerto Rico after Hurricane Maria, PLOS ONE, 14, e0218 883, https://doi.org/10.1371/journal.pone.0218883, 2019.

UNISDR: Sendai Framework for Disaster Risk Reduction 2015-2030 | UNDRR, http://www.undrr.org/publication/sendai-framework-disaster-risk-reduction-2015-2030, 2015.

U.S. Census Bureau: Building Permits Survey, https://www.census.gov/construction/bps/, 2025.

Verschuur, J., Koks, E. E., and Hall, J. W.: Port disruptions due to natural disasters: Insights into port and logistics resilience, Transportation Research Part D: Transport and Environment, 85, 102 393, https://doi.org/10.1016/j.trd.2020.102393, 2020.

Ward, P., Blauhut, V., Bloemendaal, N., Daniell, J., de Ruiter, M., Duncan, M., Emberson, R., Jenkins, S., Kirschbaum, D., Kunz, M., Mohr, S., Muis, S., Riddell, G., Schäfer, A., Stanley, T., Veldkamp, T., and Winsemius, H.: Review article: Natural hazard risk assessments at the global scale, Natural Hazards and Earth System Sciences, pp. 1–46, https://doi.org/10.5194/nhess-2019-403, 2020.

Young, R. and Hsiang, S.: Mortality caused by tropical cyclones in the United States, Nature, 635, 121–128, https://doi.org/10.1038/s41586-024-07945-5, 2024.

Zhu, L., Quiring, S. M., and Emanuel, K. A.: Estimating tropical cyclone precipitation risk in Texas, Geophysical Research Letters, 40, 6225–6230, https://doi.org/10.1002/2013GL058284, 2013.

Zscheischler, J., Westra, S., Van Den Hurk, B. J., Seneviratne, S. I., Ward, P. J., Pitman, A., Aghakouchak, A., Bresch, D. N., Leonard, M., Wahl, T., and Zhang, X.: Future climate risk from compound events, Nature Climate Change, 8, 469–477, https://doi.org/10.1038/s41558-018-0156-3, 2018.

Supplement to: Probabilistic assessment of tropical cyclone recovery burden across US Atlantic and Gulf Coast counties

Simona Meiler[1,*], Nikola Blagojević[1], Meredith Lochhead[1], Avantika Gori[2] and Jack W. Baker[1]

[1]Civil and Environmental Engineering, Stanford University, Stanford, CA, USA

[2]Department of Civil and Environmental Engineering, Rice University, Houston, TX, USA

[*]Author to whom any correspondence should be addressed: simona@simonameiler.ch

S1 Tropical cyclone hazard overview

Figure S1 shows county-level maxima of the three tropical cyclone hazards across the synthetic event set of Gori et al. (2025): wind speed, rainfall, and storm surge.

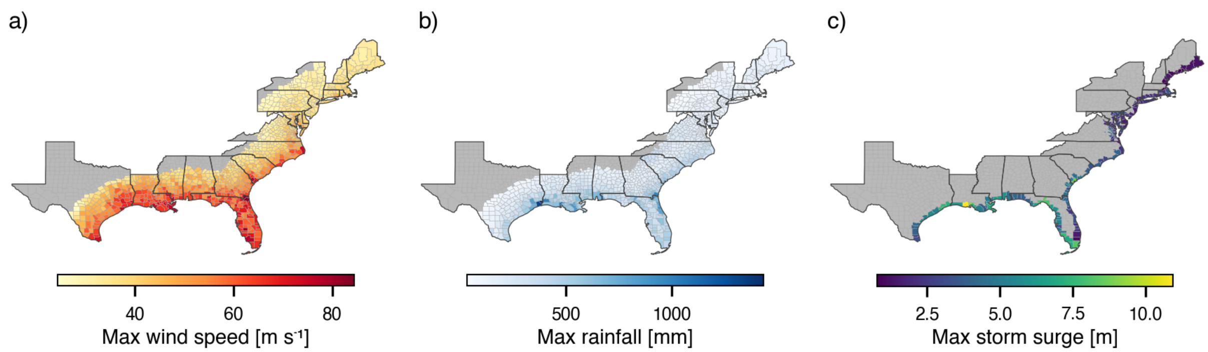

Figure S1: Tropical cyclone hazard overview for the study domain. County-level maxima across the synthetic event set of Gori et al. (2025): (a) maximum wind speed (m s^{-1}), (b) maximum total rainfall (mm), and (c) maximum storm surge (m above MHHW; coastal counties only).

S2 County-level results for Hurricane Laura (2020)

Table S1 lists all counties with modeled damage from Hurricane Laura (2020), which is discussed as a single-event example in Sect. 3.1 of the main text.

Table S1: All counties with modeled damage from Hurricane Laura (2020). Counties are sorted by scaled repair demand in weighted units affected (WUA). Raw WUA uses wind-only damage; scaled WUA includes the rain and surge scaling (Sect. 2.1.3 of the main text). Recovery burden is the modeled repair workload expressed in months of normal construction activity; higher values indicate greater repair demand relative to baseline construction capacity. Counties with zero permit capacity have undefined recovery burden (–).

County	State	WUA (scaled)	WUA (raw)	Capacity (permits/mo)	Recovery burden (months)
Calcasieu	LA	43,859	42,530	108.2	405
Beauregard	LA	19,746	14,934	6.9	2,855
Rapides	LA	7,561	7,561	19.9	380
Sabine	TX	7,182	5,538	0.0	–
Vernon	LA	7,168	7,168	2.2	3,308
Sabine	LA	6,320	6,320	4.1	1,548
Allen	LA	5,464	4,108	3.8	1,425
Cameron	LA	4,886	4,886	2.2	2,172
Orange	TX	4,293	4,293	19.6	219
Newton	TX	4,114	3,631	0.0	–
Grant	LA	3,146	3,146	0.4	7,550
Natchitoches	LA	1,742	1,742	7.9	220
Jefferson Davis	LA	1,711	1,444	5.8	298
Winn	LA	1,036	1,036	0.1	12,432
De Soto	LA	162	162	9.4	17
Shelby	TX	87	87	0.1	1,044
Red River	LA	31	31	0.4	74
Jasper	TX	18	18	3.8	5
Evangeline	LA	3	3	2.3	1
Acadia	LA	1	1	11.4	1

S3 Comparison with FEMA-verified housing damage

The damage comparison uses the OpenFEMA Housing Assistance Owners dataset (Federal Emergency Management Agency, 2025), introduced in Sect. 2.4 of the main text. We aggregate the zip-code records to county level over all declared counties. Three scope limits are relevant for the comparison. First, the dataset covers owner-occupied homes only, because renters' real property is not inspected, and registration propensity can vary with income and insurance status. Second, the dataset covers only counties designated for Individual Assistance, and designation is an administrative decision. Texas received no Individual Assistance declaration for Laura, so the three modeled Texas counties are absent from that comparison; three modeled Louisiana parishes affected by Laura were also not designated. Florida's Katrina declaration carried no Individual Assistance program, and the northeastern declarations for Ida's remnants are outside the wind field domain and are not included. Third, verified real property damage includes water-caused damage to the home. For surge- and rainfall-dominated storms, the FEMA distribution therefore includes damage components that the wind-based model captures only through the multi-hazard scaling.

For each storm, we assess the spatial damage footprint using detection, defined as the percentage of total FEMA-verified damage across all declared counties that falls in counties with non-zero modeled damage. Among counties present in both sources, we compare modeled repair demand, measured in WUA, with FEMA-verified damage using Spearman rank correlations. For the pooled comparison, we express each county's modeled and verified damage as shares of the corresponding totals across matched counties for that storm and pool the county–storm observations. We repeat the storm-specific correlations after dividing both quantities by residential exposure units to test whether the agreement is driven primarily by county size.

Table S2: Comparison of the modeled damage distribution with FEMA-verified housing damage. For each storm, scaled weighted units affected (WUA) are rank-correlated with FEMA-verified real property damage across counties present in both sources. Detection is the share of the storm's total FEMA-verified damage, summed over all declared counties, that falls in counties with non-zero modeled damage. Correlations are Spearman rank correlation coefficients (r_s) with exact two-sided p-values and are shown for $n \geq 4$. The pooled row correlates within-storm shares across all matched county–storm pairs. Hermine produced no modeled damage.

Storm	n	r_s	p	Detection
Katrina (2005)	16	+0.34	0.192	95%
Isaac (2012)	1	–	–	16%
Hermine (2016)	–	–	–	0%
Harvey (2017)	9	+0.80	0.010	4%
Irma (2017)	4	−0.60	0.400	37%
Michael (2018)	29	+0.75	< 0.001	99%
Laura (2020)	12	+0.65	0.022	92%
Ida (2021)	18	+0.40	0.097	96%
Ian (2022)	8	+0.81	0.015	82%
Pooled (within-storm shares)	96	+0.56	< 0.001	–

Observed damage is often more spatially concentrated than modeled damage. For example, Bay County accounts for 24% of Michael's modeled WUA but 58% of the FEMA-verified damage, each expressed as a share of the storm total. This concentration difference is also relevant for the Bay County recovery comparison (Sect. S4).

Table S3 tests whether the FEMA rank correlations are driven mainly by county size, repeating the comparison after dividing both modeled WUA and FEMA-verified damage by residential exposure units. The correlations are unchanged or stronger after this normalization, indicating that the agreement is not simply a county-size effect. The comparison is also insensitive to the rain and surge scaling: because the scaling is multiplicative on wind-driven damage, detection shares are identical for wind-only and scaled damage, and the rank correlations change by at most 0.03 (Sect. S7).

Table S3: Robustness of the FEMA damage-distribution comparison to county size. Left: Spearman correlation of county WUA with FEMA-verified housing damage, as in Table S2. Right: the same correlation after dividing both quantities by residential exposure units, so that damage intensities rather than totals are compared. Counties without exposure-unit data are dropped from the normalised comparison. n is the number of matched counties, r_s the Spearman rank correlation coefficient, and p the exact two-sided p-value.

	County totals			Per exposure unit		
Storm	n	r_s	p	n	r_s	p
Katrina (2005)	16	+0.34	0.192	16	+0.44	0.090
Isaac (2012)	1	–	–	1	–	–
Harvey (2017)	9	+0.80	0.010	9	+0.72	0.030
Irma (2017)	4	−0.60	0.400	4	+1.00	–
Michael (2018)	29	+0.75	< 0.001	29	+0.79	< 0.001
Laura (2020)	12	+0.65	0.022	12	+0.72	0.008
Ida (2021)	18	+0.40	0.097	18	+0.60	0.008
Ian (2022)	8	+0.81	0.015	8	+0.74	0.037

S4 Comparison with observed recovery: sensitivity and event behaviour

Table S4 reports the sensitivity of the recovery comparison to the minimum number of buildings with classified visible changes in each county–storm pair, n_{changed}. Huang et al. (2025) identify these buildings by comparing Street View images from before and after each event and classify their outcomes as an improved structure, an equivalent structure, or an empty lot. Five TCs overlap with our historical event set: Isaac (2012), Harvey (2017), Irma (2017), Michael (2018), and Laura (2020). For each county–storm pair, the rebuild rate is the share of visibly changed buildings classified as improved or equivalent, while the recovery score is the share classified as improved minus the share classified as empty lots. We use pooled Spearman rank correlations to compare baseline construction capacity with the observed rebuild rate and modeled recovery burden with the observed recovery score.

Huang et al. (2025) report county-level results for counties with at least 30 assessed buildings. We use a lower primary threshold of $n_{\text{changed}} \geq 10$ to increase the number of county–storm pairs available for the comparison and vary the filter from 0 to 30 to test the sensitivity of the results. The association between construction capacity and observed rebuild rate is positive across all filters ($r_s = +0.39$ to $+0.53$), while the association between modeled recovery burden and observed recovery score is negative across all filters ($r_s = -0.20$ to -0.41), including the stricter filter of Huang et al. Both associations become less precise as the minimum sample size increases and fewer county–storm pairs remain. We filter on the number of assessed changed buildings, the denominator of both summary measures, because it determines the precision of the estimated shares; filtering on the number of recovered buildings would condition on the recovery outcome itself and bias the comparison.

We do not report storm-specific recovery correlations because the samples are too small to be stable ($n = 2$–8 counties per storm). Laura shows a strong correct-sign association, while Michael (Fig. S2) is comparatively flat because its modeled recovery ranking is influenced by small inland Georgia counties outside the assessed, mostly coastal, building sample.

The clearest single-county disagreement is Bay County, Florida, for Michael. Bay County has the worst observed recovery outcome in the Huang et al. (2025) dataset for this storm, with an abandonment rate of 0.40, but only moderate modeled recovery burden, because the high reconstruction capacity around Panama City offsets the estimated repair demand. High abandonment is a demand-side outcome; the observed recovery state reflects social, institutional, and household-level determinants that a supply-side capacity proxy does not capture.

Table S4: Sensitivity of the comparison with Huang et al. (2025) to the minimum county sample size. The sample size is defined as the number of assessed changed buildings, n_{changed}. Spearman rank correlations are pooled across matched county–storm pairs, with exact two-sided p-values. Left: construction capacity versus observed rebuild rate. Right: recovery burden versus observed recovery score. The primary filter used in the main text is $n_{\mathrm{changed}} \geq 10$.

	Capacity vs rebuild rate			Recovery burden vs recovery score		
Filter	n	r_s	p	n	r_s	p
≥ 0	28	+0.39	0.038	27	−0.37	0.059
≥ 10	17	+0.52	0.033	17	−0.41	0.102
≥ 15	13	+0.53	0.061	13	−0.20	0.516
≥ 30	10	+0.45	0.187	10	−0.33	0.354

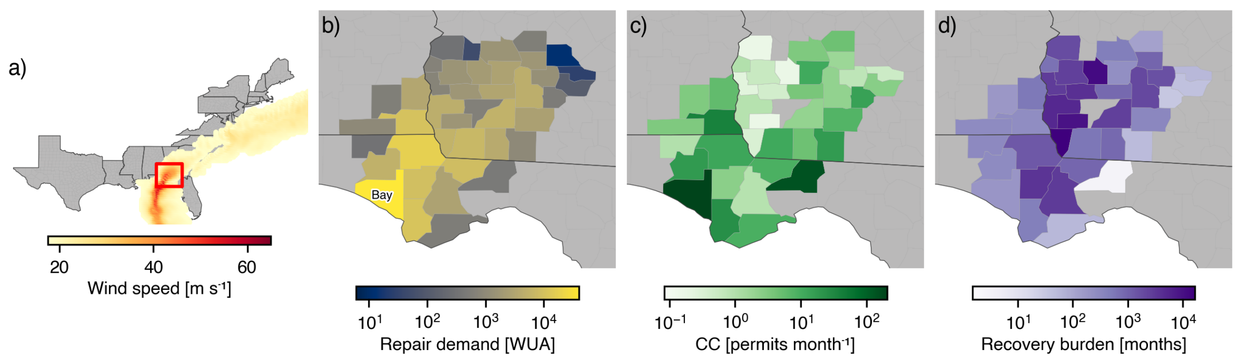

Figure S2: Repair demand and recovery burden for Hurricane Michael (2018). (a) maximum sustained wind speed (m s^{-1}), with the red box marking the focus region shown in the remaining panels; (b) repair demand, $D_{e,c}$, measured in weighted units affected (WUA), including a label for Bay County, Georgia; (c) construction capacity, C_c (CC; residential permits month^{-1}); and (d) recovery burden, $B_{e,c}$, expressed in months of baseline construction activity.

S5 Probabilistic event-set summaries

This section provides event-set summaries that complement the annual and median metrics in Sect. 3.3 of the main text. Figure S3 shows the skewness of the county-level repair-demand distributions. Figures S4 and S5 present repair demand, construction capacity, and recovery burden for each county's maximum-repair-demand event and the corresponding driver analysis. Figure S6 maps the median repair demand and recovery burden across damaging events in each county.

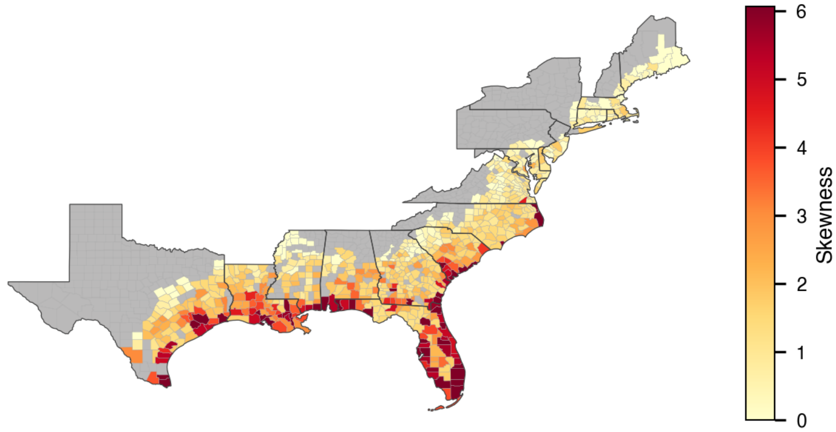

Figure S3: Skewness of tropical cyclone repair-demand distributions. Skewness is computed from the distribution of repair demand, measured in weighted units affected (WUA), across all tropical cyclones in each county. Higher values indicate more strongly right-skewed distributions, in which a small number of high-impact events contribute disproportionately to expected annual repair demand and recovery burden.

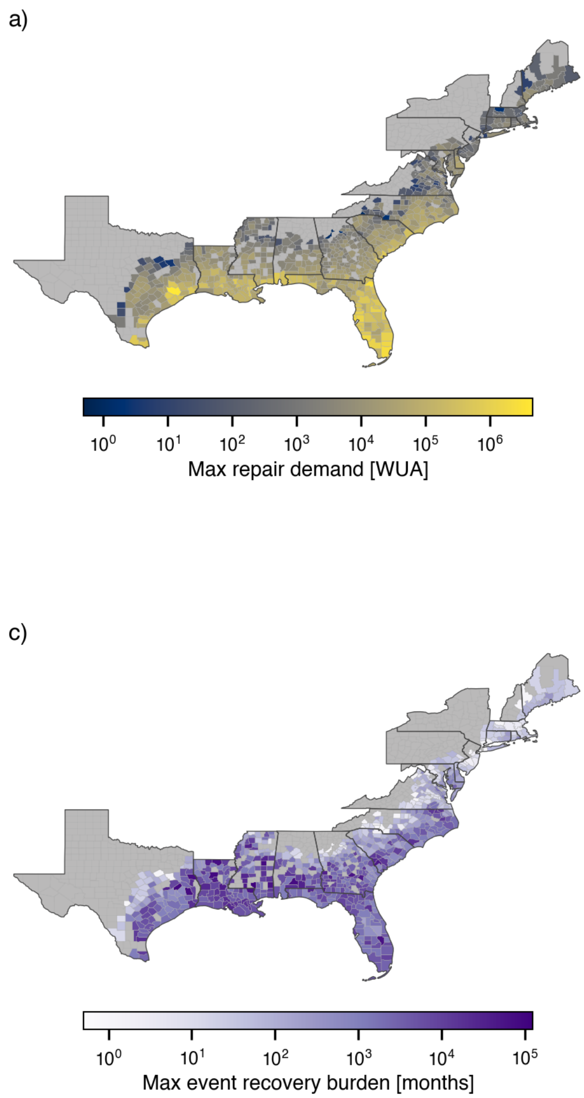

Figure S4: Maximum-event repair demand, construction capacity, and recovery burden across the US Atlantic and Gulf coasts. (a) Maximum repair demand (WUA) across the damaging events affecting each county; (b) construction capacity (CC; residential permits month^{-1}); and (c) recovery burden for the county's maximum-repair-demand event, expressed in capacity-equivalent months. The maximum-repair-demand event is identified separately for each county; the maps therefore do not represent a single spatially coherent synthetic TC.

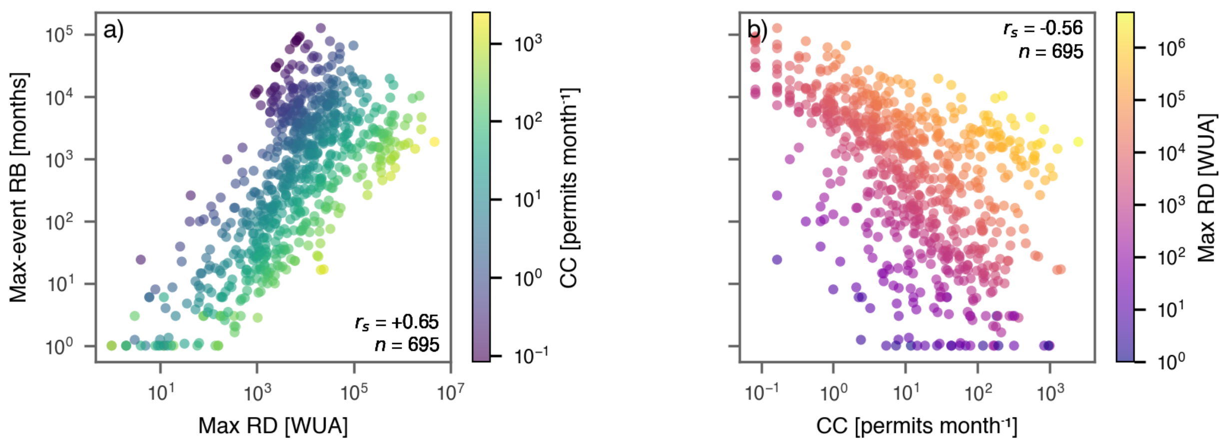

Figure S5: Drivers of maximum-event recovery burden. (a) Recovery burden (RB) for each county's maximum repair demand (RD) event, colored by construction capacity (CC; residential permits month^{-1}); and (b) maximum-event recovery burden versus construction capacity, colored by maximum repair demand. Maximum-event metrics are computed separately for each county from its local distribution of damaging events. Spearman rank correlations (r_s) and the number of counties with available data (n) are shown in each panel.

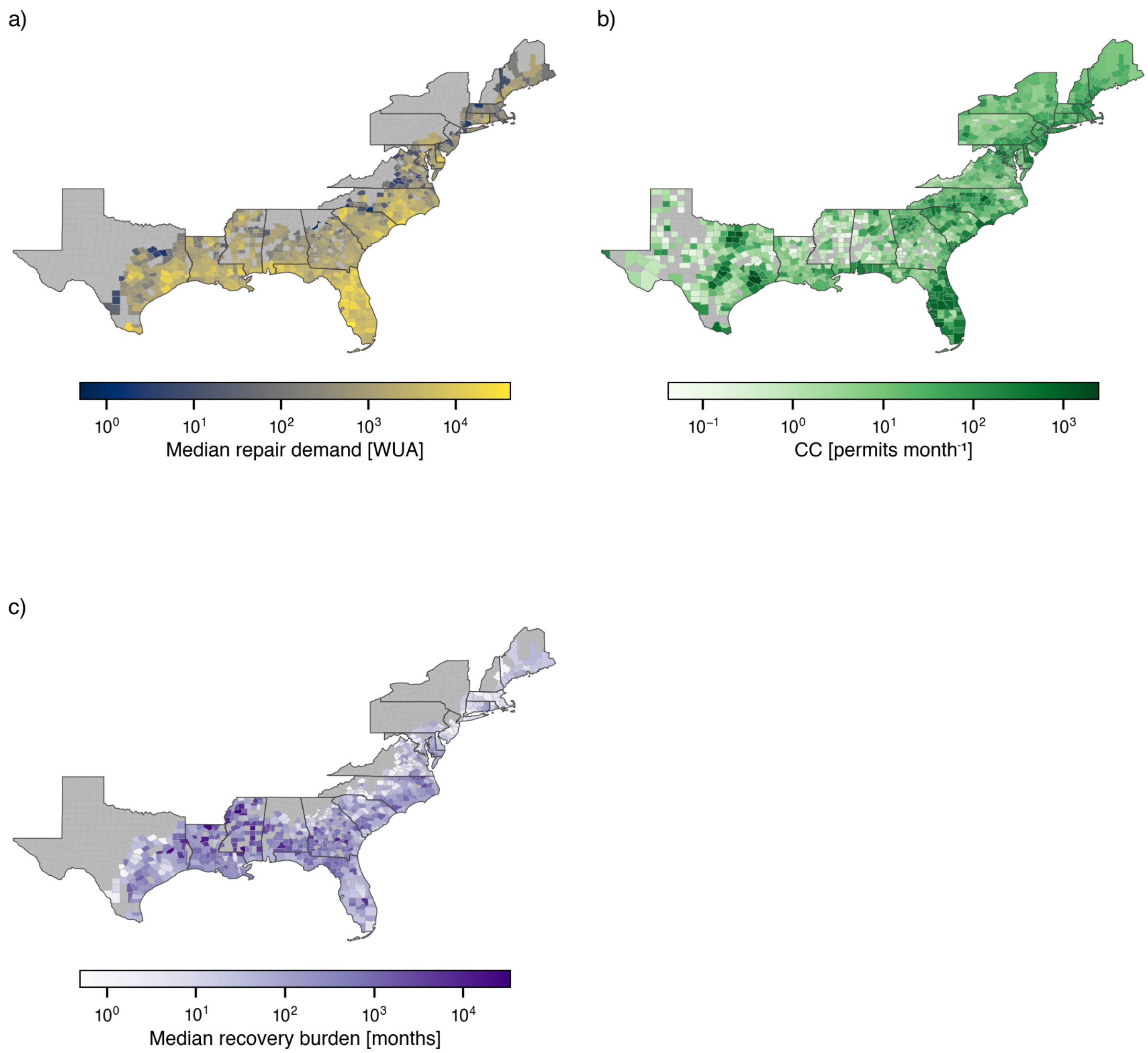

Figure S6: Median repair demand, construction capacity, and recovery burden across the US Atlantic and Gulf coasts. (a) Median repair demand (WUA) across the damaging events affecting each county; (b) construction capacity (CC; residential permits month^{-1}); and (c) median recovery burden across damaging events, expressed in capacity-equivalent months. Repair demand and recovery burden medians are calculated separately for each county and need not correspond to the same event. The maps therefore summarize typical county-level outcomes rather than a single spatially coherent synthetic TC.

S6 Comparison with the FEMA National Risk Index

We compare our estimates with the county-level FEMA National Risk Index (NRI, 2025 release) for the 695 counties in the analysis sample. We use the Hurricane and Coastal Flooding expected annual loss fields (HRCN_EALB, HRCN_EALT, and CFLD_EALT) as risk references, and the Community Resilience and Social Vulnerability scores (RESL_SCORE and SOVI_SCORE) as resilience and vulnerability references. Because the NRI expected annual loss is monetary, we additionally compute expected annual repair cost (EARC) by applying the annual aggregation used for expected annual repair demand (EARD) to repair costs, obtained by multiplying fractional building damage by replacement value and aggregating by county and event before frequency weighting. We report Spearman rank correlations because both sets of metrics are heavy-tailed and evaluated as county ranks; recovery metrics enter as recovery burden, so positive correlations indicate greater burden. To assess whether the association with Social Vulnerability is explained by underlying probabilistic damage risk, we compute rank-based partial correlations between median damaging-event recovery burden and Social Vulnerability, controlling for either modeled EARD or NRI hurricane expected annual loss.

The results are summarized in Table S5 and reported in Sect. 3.5 of the main text. EARC ranks counties similarly to the NRI hurricane building and wind expected annual losses ($r_s = 0.63$–0.65, $n = 687$; Pearson correlations on $\log_{10}$-transformed values 0.64–0.66), and adding coastal flooding to the NRI hurricane loss does not improve the agreement, consistent with a damage model that includes rainfall and surge only through a scaling factor. The unit-based EARD gives nearly identical rank agreement ($r_s = +0.63$–0.64), so the comparison is not sensitive to whether modeled impacts are expressed as housing units or repair costs. Of the 60 counties in the highest tercile of TC risk and the lowest tercile of construction capacity, 35 (58%) fall in the highest Social Vulnerability tercile and 37 (62%) in the lowest Community Resilience tercile; the 12 counties that fall into neither group are listed in Table S6.

Table S5: Comparison of risk and recovery estimates with the FEMA National Risk Index (NRI). Panel A compares the modeled monetary risk estimate (expected annual repair cost, EARC) with NRI expected annual loss (EAL) metrics. Panel B reports rank correlations between modeled quantities and the NRI Community Resilience and Social Vulnerability scores; higher recovery burden indicates greater repair demand relative to baseline construction capacity. Panel C re-estimates the association with Social Vulnerability after controlling for probabilistic damage risk, using either modeled EARD or NRI hurricane EAL as the control. Entries are Spearman rank correlation coefficients (r_s); Panel A also lists Pearson correlation coefficients (r) on $\log_{10}$-transformed values. All coefficients are significant at $p < 0.01$ unless marked. The analysis sample comprises the 695 US Atlantic and Gulf coast counties with positive modeled risk, recovery burden and construction capacity. Comparisons against NRI expected annual loss cover 687 of these counties, because the NRI 2025 release reports Connecticut on the nine planning regions that replaced counties as county equivalents and therefore provides no expected annual loss for the eight legacy Connecticut counties used here; the Community Resilience and Social Vulnerability scores for those counties are housing-unit weighted averages of the overlapping planning regions.

Panel A. Modeled monetary risk vs FEMA NRI monetary risk			
	r_s	r ($\log_{10}$)	n
EARC vs NRI hurricane building EAL	+0.63	+0.64	687
EARC vs NRI hurricane wind EAL	+0.65	+0.66	687
EARC vs NRI wind + coastal-flood EAL	+0.63	+0.64	687
Panel B. Recovery burden vs NRI resilience and social vulnerability indices (Spearman r_s)			
	Community Resilience	Social Vulnerability	Hurricane EAL (damage risk)
Construction capacity	+0.42	−0.62	+0.47
EARB (expected annual recovery burden)	−0.36	+0.47	+0.29
Median damaging-event recovery burden	−0.44	+0.56	−0.11
Panel C. Social Vulnerability associations controlling for damage risk (Spearman r_s)			
	raw	partial (control EARD)	partial (control wind EAL)
Construction capacity	−0.62	−0.65	−0.63
Median damaging-event recovery burden	+0.56	+0.56	+0.55

Table S6: Priority counties outside the NRI Social Vulnerability and Community Resilience tercile groupings. Priority counties are those in both the highest tercile of tropical cyclone risk and the lowest tercile of construction capacity within the analysis sample. The 12 counties listed here meet this definition but are not in either the highest tercile of the NRI Social Vulnerability score or the lowest tercile of the NRI Community Resilience score. Counties are sorted by number of housing units. Pop. % of state is the percentage of the state population living in the county. Permits per month is the construction capacity proxy, and permits per 1000 units normalizes it by housing stock. NRI scores are county percentile scores from 0 to 100; higher Social Vulnerability indicates greater vulnerability, whereas higher Community Resilience indicates greater resilience.

County	State	Housing units	Pop. % of state	Permits per month	Permits per 1000 units	NRI SVI	NRI Resil.
Cameron	Louisiana	3,582	0.12	2.25	0.628	45	99
Union	Florida	5,293	0.07	3.75	0.708	39	32
Seminole	Georgia	5,969	0.09	0.33	0.056	48	33
Grant	Louisiana	9,228	0.48	0.42	0.045	58	39
Allen	Louisiana	9,880	0.49	3.83	0.388	61	39
Appling	Georgia	10,125	0.17	0.33	0.033	74	49
Pike	Alabama	18,021	0.66	3.50	0.194	74	58
Ware	Georgia	19,934	0.34	3.75	0.188	78	81
Lamar	Mississippi	27,228	2.17	3.75	0.138	56	56
St. Mary	Louisiana	29,762	1.06	3.08	0.104	76	88
Jones	Mississippi	33,761	2.27	1.92	0.057	78	41
Victoria	Texas	43,846	0.31	3.58	0.082	59	64

S7 Effect of multi-hazard scaling

We evaluated the influence of the multi-hazard scaling by comparing the default scaled calculation with a wind-only counterfactual. In the wind-only specification, the building-level wind losses, $L_{e,b}^{\text{wind}}$, were assigned directly to damage states. In the scaled specification, the same wind losses were transformed using the county–event scaling factor $\alpha_{e,c}$ according to Equation (2) of the main text of the main text. Both specifications therefore use the same building inventory, wind hazard, impact functions, damage-state thresholds, repair-demand weights, event frequencies, and construction-capacity estimates. The comparison isolates the effect of the rainfall and storm-surge scaling on the downstream analysis.

We first quantified the direct effect of scaling on EARD. For each county, we calculated the ratio of scaled to wind-only EARD. We also calculated the expected annual number of housing-unit occurrences in each damage state and their contribution to repair demand after applying the damage-state weights $(w_1, w_2, w_3, w_4) = (1, 1, 3, 6)$. County ratios are undefined where wind-only EARD is zero; these counties are shown in gray in Fig. S7.

To determine whether the main conclusions depend on the scaling, we repeated the analyses underlying Figures 3 and 4 of the main text using wind-only damage. We compared the resulting county metrics using Spearman rank correlations. Following the main analysis, we classified priority counties within each specification as those simultaneously in the highest tercile of EARD and the lowest tercile of construction capacity among eligible counties. Tercile thresholds were recalculated separately for the wind-only and scaled specifications, and agreement between the resulting priority sets was measured using the Jaccard index, defined as the size of their intersection divided by the size of their union. We also repeated the historical comparison with FEMA-verified housing damage using wind-only and scaled repair demand.

The scaling increased total EARD from 238,995 to 264,196 WUA yr^{-1}, an increase of 10.5%. Its effect was strongly concentrated in the more severe damage states (Fig. S7b). Relative to the wind-only calculation, expected annual housing-unit occurrences changed by approximately −8 in DS1, +195 in DS2, +1,787 in DS3, and +3,275 in DS4, corresponding to relative changes of −0.04%, +1.0%, +4.5%, and +24.8%, respectively. After applying the damage-state weights, DS3 and DS4 accounted for 99.3% of the increase in repair demand, with DS4 alone accounting for 78.0%. The scaling therefore affects repair demand primarily by increasing the occurrence of severe damage rather than by substantially increasing the total number of slightly damaged housing units.

The damage-state transitions show the same pattern. Of the housing-unit occurrences classified as DS1 under wind-only damage, 24.0% shifted to DS2 after scaling. Similarly, 26.2% of wind-only DS2 occurrences shifted to DS3, and 8.3% of wind-only DS3 occurrences shifted to DS4. Only 0.25% of DS0 occurrences crossed into DS1. These transitions explain why the effect on weighted repair demand is considerably larger than the change in the number of affected housing-unit occurrences: crossings into DS3 and DS4 increase the repair-demand weight from 1 to 3 or 6.

Scaling has a comparable but slightly larger effect on the sum of county-level EARB, which increases by 11.8%, compared with 10.5% for EARD. The difference reflects how the metrics are aggregated: EARD sums repair demand directly across counties, whereas EARB first expresses each county-event's burden relative to local construction capacity and then sums the resulting county-level indices (Fig. S7b).

Despite this effect on damage severity, the principal county-level results were highly robust (Table S7). Rank correlations between wind-only and scaled county metrics ranged from 0.963 to 0.998, and the correlations reported in Fig. 4 changed by no more than 0.009. The wind-only specification identified 56 priority counties, all of which remained priorities under the scaled specification. Scaling added four counties—Dougherty and Toombs Counties, Georgia, and Jim Wells and Live Oak

Counties, Texas—giving a Jaccard similarity of 0.933 between the two priority sets. The 12 priority counties reported in Table S6 were unchanged.

The historical damage comparison likewise provides no evidence that scaling improves agreement with observations. Damage-footprint detection was identical under the two specifications for every historical storm, and the pooled Spearman correlation with FEMA-verified housing damage changed only from $r_s = 0.557$ for wind-only damage to $r_s = 0.559$ for scaled damage. The scaling should therefore be interpreted as a computationally tractable representation of the potential additional repair demand associated with rainfall and storm surge, rather than as a demonstrated improvement in damage-estimation accuracy.

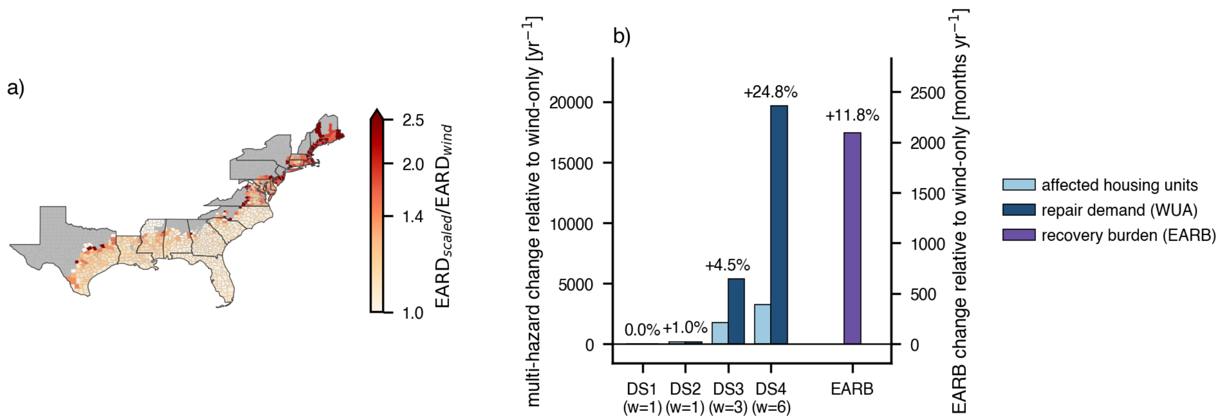

Figure S7: Effect of multi-hazard scaling on expected annual repair demand and recovery burden. (a) Ratio of scaled expected annual repair demand, $\mathrm{EARD_{scaled}}$, to wind-only expected annual repair demand, $\mathrm{EARD_{wind}}$, by county. Counties with zero wind-only EARD are shown in gray because the ratio is undefined. Ratios of 2.5 or greater are represented by the upper end of the color scale; large ratios can arise where wind-only EARD is small. (b) Change relative to the wind-only calculation in the expected annual number of affected housing units in each damage state (light bars; housing units yr^{-1}), the corresponding repair demand (dark bars; WUA yr^{-1}), and expected annual recovery burden. Percentages indicate the relative change in affected housing units within each damage state. Repair-demand weights are 1 for DS1 and DS2, 3 for DS3, and 6 for DS4. Across all damage states, scaling increased total EARD by 10.5% and total EARB by 11.8%.

Table S7: Effect of multi-hazard scaling and robustness of the principal results. Panel A reports the change in total expected annual repair demand and in the pooled historical comparison with FEMA-verified housing damage. Panel B reproduces the four Spearman relationships reported in Fig. 4 under the wind-only and scaled specifications; the difference is scaled minus wind-only. Panel C reports cross-specification rank agreement for the principal county metrics and agreement in the county classifications. The wind-only analysis sample contains 676 counties with positive modeled risk, recovery burden, and construction capacity, compared with 695 under scaling.

Panel A. Overall effect and historical comparison

Quantity	Wind only	Scaled	Change
Expected annual repair demand (WUA yr^{-1})	238,995	264,196	+10.5%
FEMA-verified damage, pooled within-storm shares (r_s, $n = 96$)	+0.557	+0.559	+0.001

Panel B. Relationships reported in Fig. 4

Relationship	Wind-only r_s	Scaled r_s	Difference
EARB versus EARD	+0.773 ($n = 676$)	+0.778 ($n = 695$)	+0.005
EARB versus construction capacity	−0.479 ($n = 676$)	−0.485 ($n = 695$)	−0.006
Median recovery burden versus median repair demand	+0.390 ($n = 676$)	+0.385 ($n = 695$)	−0.005
Median recovery burden versus construction capacity	−0.722 ($n = 676$)	−0.731 ($n = 695$)	−0.009

Panel C. Stability of county-level outputs and classifications

County-level output	Cross-specification agreement	Sample size
EARD ranks	$r_s = +0.998$	$n = 734$
EARB ranks	$r_s = +0.998$	$n = 676$
Median repair-demand ranks	$r_s = +0.963$	$n = 676$
Median recovery-burden ranks	$r_s = +0.981$	$n = 676$

Classification	Wind only	Scaled	Agreement
Eligible analysis counties	676	695	19 additional
Priority counties	56	60	56 common; $J = 0.933$
Counties reported in Table S6	12	12	12 common; $J = 1.000$

References

Federal Emergency Management Agency: OpenFEMA Dataset: Housing Assistance Program Data – Owners – V2, https://www.fema.gov/openfema-data-page/housing-assistance-program-data-owners-v2, 2025.

Gori, A., Lin, N., Chavas, D., Oppenheimer, M., and Xian, S.: Sensitivity of Tropical Cyclone Risk across the US to Changes in Storm Climatology and Socioeconomic Growth, Environmental Research Letters, 20, 064 050, https://doi.org/10.1088/1748-9326/add60d, 2025.

Huang, T., Zanocco, C., Wang, Z., Hwang, J., and Rajagopal, R.: Built Environment Disparities Are Amplified during Extreme Weather Recovery, Nature, 648, 349–356, https://doi.org/10.1038/s41586-025-09804-3, 2025.